© 2021. Published by The Company of Biologists Ltd | Development (2021) 148, dev193755. doi:10.1242/dev.193755

RESEARCH ARTICLE

Symmetry and fluctuation of cell movements in neural crest-derived facial mesenchyme

Adrian Danescu[1], Elisabeth G. Rens[2,*], Jaspreet Rehki[1], Johnathan Woo[1], Takashi Akazawa[1,‡], Katherine Fu[1], Leah Edelstein-Keshet[2] and Joy M. Richman[1,§]

ABSTRACT

In the face, symmetry is established when bilateral streams of neural crest cells leave the neural tube at the same time, follow identical migration routes and then give rise to the facial prominences. However, developmental instability exists, particularly surrounding the steps of lip fusion. The causes of instability are unknown but inability to cope with developmental fluctuations are a likely cause of congenital malformations, such as non-syndromic orofacial clefts. Here, we tracked cell movements over time in the frontonasal mass, which forms the facial midline and participates in lip fusion, using live-cell imaging of chick embryos. Our mathematical examination of cell velocity vectors uncovered temporal fluctuations in several parameters, including order/disorder, symmetry/asymmetry and divergence/convergence. We found that treatment with a Rho GTPase inhibitor completely disrupted the temporal fluctuations in all measures and blocked morphogenesis. Thus, we discovered that genetic control of symmetry extends to mesenchymal cell movements and that these movements are of the type that could be perturbed in asymmetrical malformations, such as non-syndromic cleft lip.

This article has an associated 'The people behind the papers' interview.

KEY WORDS: Craniofacial, Avian embryo, Frontonasal, Fluctuating asymmetry, Mathematical analysis, Live cell imaging, Organ culture, Actomyosin

INTRODUCTION

Facial morphogenesis requires successful passage through multiple delicate steps that must be perfectly orchestrated to give rise to the bilaterally symmetrical adult form. There is a tolerance for a certain amount of variation or developmental instability in the early stages of embryogenesis so that in the majority of individuals, developmental abnormalities do not occur. However, more significant disturbances will lead to congenital malformations, such as cleft lip with or without cleft palate, the most common craniofacial abnormality in humans (Beames and Lipinski, 2020). The typical orofacial cleft is an isolated or non-syndromic condition known as non-syndromic cleft lip with or without cleft palate (NSCLP) (Beaty et al., 2016). The etiology of NSCLP is multifactorial, involving additive effects of multiple gene variants and interplay with environmental factors. The evidence from large studies on facial clefting shows that gene variants contribute to only 30% of the risk of NSCLP, the rest being the result of environmental stresses (Ludwig et al., 2017). The key role of environment is further highlighted by the disconcordance for cleft lip in 50-60% of monozygotic twin pairs (Grosen et al., 2011; Leslie et al., 2017).

The theory of developmental instability is that it is a continuum and is inherited to some degree (Van Dongen, 2007). The main way to measure developmental instability is via right-left symmetry comparisons (Ekrami et al., 2020, 2018). The greater the fluctuation or randomness of the asymmetry (no right or left predominance), the greater the developmental instability. These fluctuations in symmetry are different to the asymmetry caused by a specific insult, such as a unilateral injury or infection. In NSCLP, the prediction is that relatives of individuals with clefts should have more fluctuating asymmetry compared with control populations. This hypothesis has been tested by several groups. Surface scans of adult faces showed significant asymmetries in specific parts of the face in unaffected relatives compared with controls (Roosenboom et al., 2017; Weinberg et al., 2009; Zhang et al., 2018). There is also increased variation in skeletal morphology (Ceuninck and Starbuck, 2019) that correlated with increased risk of facial clefting (Richmond et al., 2018). These data reinforce the hypothesis that developmental instability exists in the embryo and that sometimes buffering is inadequate and a cleft will result (Thornhill and Møller, 1997). In this study, we sought to understand the sources of developmental instability in the upper face at the cellular level.

The origins of the face begin in the cranial neural crest cells that begin to migrate out from the neural plate at 3 weeks gestation (O'Rahilly and Müller, 2007) and move into the ventral side of the embryo where the face will form. The right and left streams of neural crest cells migrate and are patterned independently of each other. Although some preprogramming is present in premigratory neural crest cells, as shown by quail-chicken chimeras, most of the Hox-negative facial neural crest is interchangeable (Couly et al., 2002; Noden, 1978). Hox-negative cranial neural crest cells are the key repository of patterning information for the jaws (Couly et al., 1993; Noden, 1978; Schneider, 2018; Schneider and Helms, 2003). Hence, a decrease in survival or proliferation of neural crest cells will lead to a bilateral or unilateral reduction in the size of the jaws as observed in Treacher Collins syndrome, hemifacial macrosomia or after exposure to ethanol (Vega-Lopez et al., 2018). Thus, one reason for developmental instability is the variation in neural crest cell migration and proliferation on the right versus the left side of the face.

[1]Life Sciences Institute, 2350 Health Sciences Mall, University of British Columbia, Vancouver, V6T 1Z3, Canada. [2]Department of Mathematics, University of British Columbia, 1986 Mathematics Road, Vancouver, V6T 1Z2, Canada.
*Present address: TU Delft Institute for Computational Science and Engineering, Mekelweg 4, 2628 CD Delft, The Netherlands. ‡Present address: School of Food Industrial Sciences, Miyagi University, 2-2-1 Hatadate, Taihaku-ku, Sendai City Miyagi Prefecture, Japan 982-0215.

§Author for correspondence (richman@dentistry.ubc.ca)

L.E.-K., 0000-0002-2233-690X; J.M.R., 0000-0002-1409-8163

Handling Editor: Paul François
Received 12 June 2020; Accepted 5 March 2021

Development (2021) 148, dev193755. doi:10.1242/dev.193755

Once the neural crest-derived mesenchyme reaches the presumptive face, frontonasal, maxillary, lateral nasal and mandibular buds begin to grow out to surround the oral cavity. In order to make the upper lip, three of the facial prominences need to fuse together: the frontonasal mass (equivalent to mammalian medial nasal prominences), and maxillary and lateral nasal prominences. A series of developmental events need to occur: contact between the facial prominences, adhesion of epithelial surfaces, breakthrough of the mesenchyme to form a bridge; and proliferation of the mesenchyme to fill out residual grooves (Abramyan and Richman, 2015). Disruption at any stage will cause unilateral cleft lip (NSCL), the most common type of non-syndromic orofacial cleft (Gundlach and Maus, 2006; Leslie and Marazita, 2013). Developmental instability in the embryonic face at the cellular level may allow environmental factors to alter development on one side of the face, leading to a spectrum of facial abnormalities, from mild asymmetry to cleft lip with or without cleft palate (Richmond et al., 2018). Indeed, precise comparisons of lip fusion in several mouse strains (normal and cleft lip liable) found that the timing of when fusion was initiated was more variable in the cleft lip-liable strains (Wang et al., 1995). There is also asymmetry of the jaw skeleton, derived from cranial neural crest cells in the normal human fetus (Katsube et al., 2019).

Studies in mouse models have clearly shown that even when the genetics is precisely controlled, there is incomplete penetrance of cleft lip. In the majority of craniofacial studies, unilateral cleft lip is induced but only in a subset of embryos (Everson et al., 2017; Ferretti et al., 2011; Jin et al., 2012; Juriloff and Harris, 2008; Losa et al., 2018; Parsons et al., 2008; Song et al., 2009). All of these studies were performed using static observations at discrete time points (usually 12 h apart); therefore, the dynamic transition between stages was not observed. Closely timed observations need to be made as well as measurements on both sides of the face (Wang et al., 1995) as there may be an increase in fluctuating asymmetry at an early stage prior to lip fusion.

The hypothesis we explore here is that fluctuating asymmetry occurs at the cellular level and particularly in the mesenchyme. There is evidence from several types of static studies that a degree of cell movement is present in facial mesenchyme. Focal labeling studies carried out with ^{3}H-thymidine (Patterson et al., 1984), dye spots (Lee et al., 2004; McGonnell et al., 1998), transfection with GFP plasmids (Geetha-Loganathan et al., 2014) or genetically labeled mouse embryos (Kaucka et al., 2016; Tao et al., 2019) report gradual spreading of the label. However, in these studies, cell spread is due to a mix of proliferation, cell migration and displacement. To date, only one live-imaging experiment has been conducted on the face in a mouse model (Tao et al., 2019) but the future lip was not examined.

In the present study, we used a chicken embryo model in which live imaging has been carried out in several different contexts (although not the face) (Bénazéraf et al., 2017; Gros et al., 2010; Kulesa et al., 2010; McColl et al., 2018; Voiculescu et al., 2007). Here, we imaged the frontonasal mass in organ culture because this prominence contained the facial midline and is the region affected in NSCLP. Using high-resolution live imaging, we captured the movements of mesenchymal cells across the entire prominence. We used unbiased mathematical approaches and detected fluctuations in cell behaviors over time. We also demonstrate that disruption of the actomyosin network causes a loss of temporal fluctuations, causing a loss of symmetry and uncoordinated cell movements. We suggest that a certain level of cell movement is normal but that there are times when these movements change. It is at these points of change when the face may be susceptible to an environmental insult.

RESULTS

Convergence-extension is a part of normal frontonasal morphogenesis

We used the chicken embryo for our studies because the neural crest cell contributions to the face have been determined and because the midface appears to be more similar to that of human (Diewert and Lozanoff, 1993) than the mouse, which has a deep midline furrow (Hu and Marcucio, 2009b). We began by characterizing the key shape changes during frontonasal mass morphogenesis for live-imaging experiments. Scans of whole chicken heads covering stages 24-29 (Hamburger and Hamilton, 1951), equivalent to human morphogenesis at 6-7 weeks gestation (Richman and Vora, 2017), were reconstructed (Fig. 1A-C′). The linear 3D and 2D measurements of the frontonasal mass showed that there were complex changes in the distance between the nasal slits depending on embryonic stage and position (Fig. 1A′-C′,D,E; Fig. S1). The head increased in width by 38% whereas the absolute distance between the nasal slits decreased significantly (Fig. S1). The dorso-ventral thickness of the frontonasal mass mesenchyme also increased (Fig. 1G) as did the volume (3D segmentations; Fig. 1F; Fig. S2A). During the same period, proliferation is known to increase, particularly near the tip of the beak as a prelude to defining upper beak morphology (Wu et al., 2006).

To identify more specifically where shape changes were occurring, we carried out landmark-based 3D geometric morphometrics (Klingenberg, 2011) on segmented frontonasal masses (landmarks shown in Fig. 1B and Fig. S2A). Principal component analysis showed a separation of the shape by stage (Procrustes ANOVA, P<0.0001; Fig. S2B). Most of the variation (81.5%) was present in component 1 (Fig. S2C). Between stages 24 and 28, there was medial displacement of the lateral landmarks and extension of the cranial-caudal landmarks with minimal extension in the dorsoventral axis (Fig. 1H-J). By stage 29, there was significant extension in both the dorsoventral (Fig. 1K,L) and craniocaudal (Fig. 1M) axes with convergence in the medial axis (Fig. 1M). We also compared average centroid size and found that there were significant shape changes only between stage 29 and stage 24 (Fig. S2D).

The shape changes, particularly at stage 29, could have been driven by the differentiation of the prenasal cartilage, a derivative of the frontonasal mass (Richman and Tickle, 1989). We mapped SOX9 expression, one of the earliest markers of chondroprogenitor cells (Celá et al., 2016) as well as COL2A1, the main matrix component of cartilage. There was diffuse expression of SOX9 at stage 24 (Fig. 2A) but by stage 26 there was a central expression domain overlapping the future region of the prenasal cartilage condensation (Fig. 2B), which became more defined at stage 28 (Fig. 2C). The SOX9 expression suggested early commitment of midline cells to a chondrogenic fate. However, there was a delay before COL2A1 was expressed (Fig. S3A,B). No signal was detected at stage 29; therefore, secretion of matrix was not a main driver of shape changes.

Orientation of cell division does not explain extension of the frontonasal mass

One of the mechanisms of morphogenesis is oriented cell division, whereby progeny are preferentially produced in one axis. We predicted that there would be many cells that would divide in the cranio-caudal plane, where the most extension was observed (Fig. 1J). However, unexpectedly, mesenchymal cells were observed dividing in the perpendicular, mediolateral plane (Fig. 2D′-G). There did not seem to be a right or left preference for cells dividing at specific angles (Fig. S4). Not all cells could be scored because some were in prophase or perhaps were dividing in the perpendicular plane. We therefore sectioned other embryos in the coronal plane and found that there were significantly

Development (2021) 148, dev193755. doi:10.1242/dev.193755

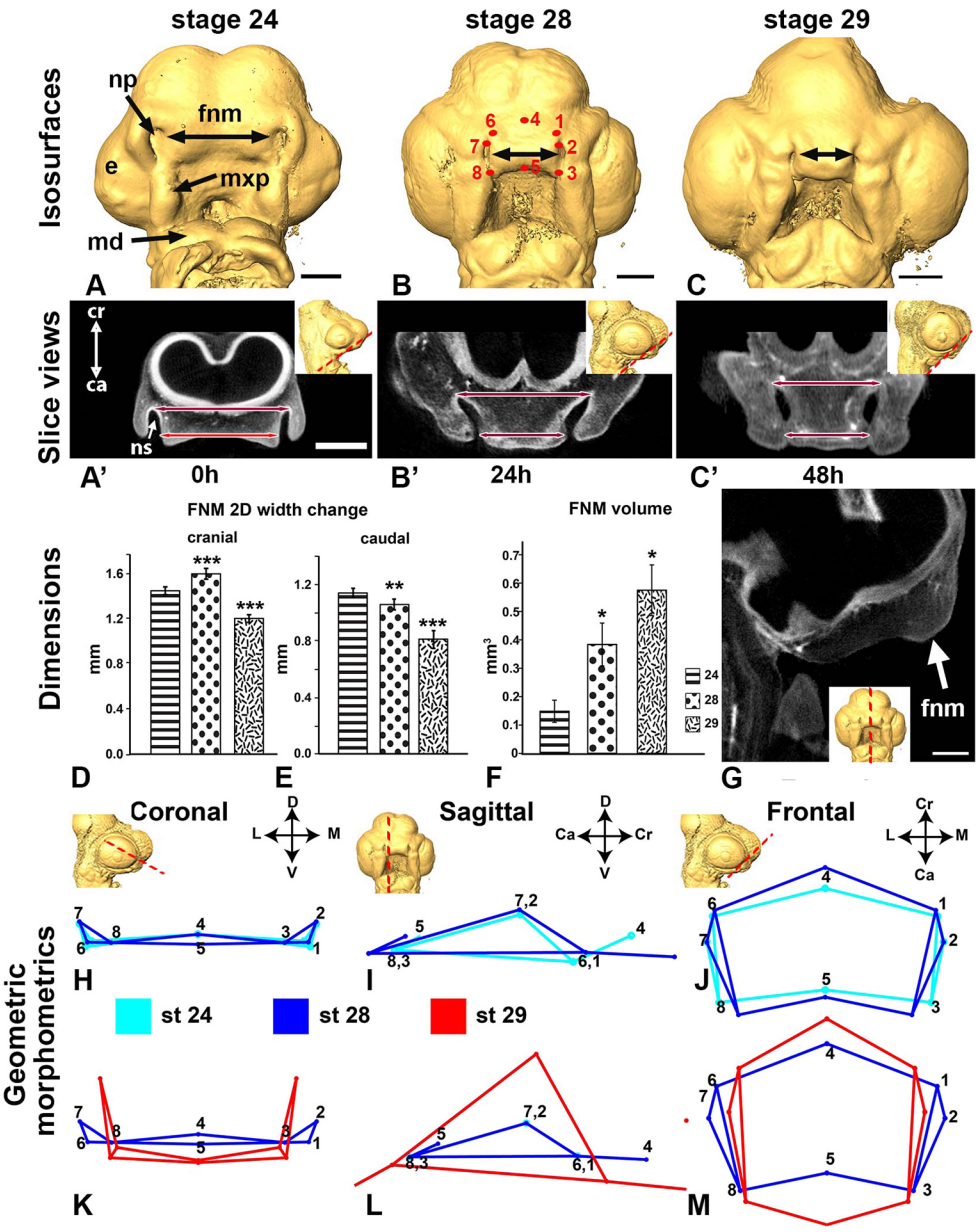

Fig. 1. *In vivo* morphogenesis of the chicken embryo face. Analysis using 2D and 3D morphometrics pinpoints the stages when major narrowing and outgrowth of upper beak takes place. (A-C) Between stage 24 and 29 the nasal slits are gradually relocated more medially in the frontonasal mass. (A′-C′) Slice views through the frontonasal mass (as shown by the dashed lines in insets) show maximum and minimum distance between the nasal slits (double-headed arrows). (D,E) Absolute distance significantly decreases with increasing stage. (F) Volumetric increases in the frontonasal mass. (G) Stage 28 embryo showing increased outgrowth in the dorsoventral axis. Dashed line in inset shows midsagittal plane of the slice view. (H-M) Wireframes showing mean displacement of eight homologous 3D landmarks for three stages of development (see B for landmark positions). (H-J) Stage 24-28 differences were mainly observed in the craniocaudal and mediolateral axes. (K-M) The displacement of landmarks was significant in all three axes. Scale bars: 500 µm (in A′ for A-C′);. 250 µm (G). Ca, caudal; Cr, cranial; D, dorsal; e, eye; fnm, frontonasal mass; L, lateral; M, medial; md, mandibular prominence; mxp, maxillary prominence; np, nasal pit; ns, nasal slit; V, ventral. **P*<0.05, ***P*<0.01, ****P*<0.001 (one-way ANOVA with Tukey's post-hoc test, *n*=8 for each stage in D-F,H-M).

fewer nuclei with visible division planes compared with the frontal sections [frontal, *n*=6, 18.4±3.0% mitotic cells in MATC (metaphase, anaphase, telophase and cytokinesis); coronal *n*=6, 7.3%±1.84 mitotic cells in MATC; two sample equal variance, two-tailed *t*-test, *P*<0.0001]. This decrease in scoreable cells in the coronal plane may mean that we missed cells that were dividing in the craniocaudal axis. New cells are added preferentially to the lateral edges of the frontonasal mass, likely under the stimulation of signals from the nasal slit (Szabo-Rogers et al., 2008). As oriented cell division does not contribute to midfacial extension, we investigated whether growth of the surrounding structures, such as the eyes and brain, indirectly caused the frontonasal mass to narrow and extend.

In vitro cultures of the face demonstrate that the frontonasal mass undergoes morphogenesis independently of the eyes and brain

How much of frontonasal mass morphogenesis is intrinsically regulated? In the chicken embryo, there are well-documented signals that come from the brain to set up the face at early stages. *SHH* is expressed in the floorplate of the diencephalon and this signal is required to induce the frontonasal mass epithelial growth zone that controls morphogenesis (Hu and Marcucio, 2009a; Young et al., 2010). The epithelial growth zone itself is capable of inducing a branched upper beak (Hu et al., 2003). Initially, we dissected the frontonasal mass with the brain and eyes, always including the frontonasal epithelial zone, and placed it into culture (Fig. 3A,B). The readout for morphogenesis was the decrease in internasal distance. As seen *in vivo*, the frontonasal mass narrowed *in vitro* (*n*=12; a decrease of 30% by 48 h compared with 0 h; Fig. 3C-C″,F). Surprisingly, the narrowing rate was not changed significantly when the eyes and brain were removed (*n*=12; Fig. 3D-D″,F). We also removed the maxillary and mandibular prominences, leaving just the nasal slits, frontonasal mass and lateral nasal prominences. Again, narrowing still took place (Fig. S5A-H). Thus, the frontonasal mass grown with the epithelium was able to undergo morphogenesis independently of signals from the brain or the eyes. The width of the frontonasal mass in the organ cultures tracked very closely to the *in vivo* dimensions of stage 24, 28 and 29 embryos (Fig. 3G; Fig. S1).

Development (2021) 148, dev193755. doi:10.1242/dev.193755

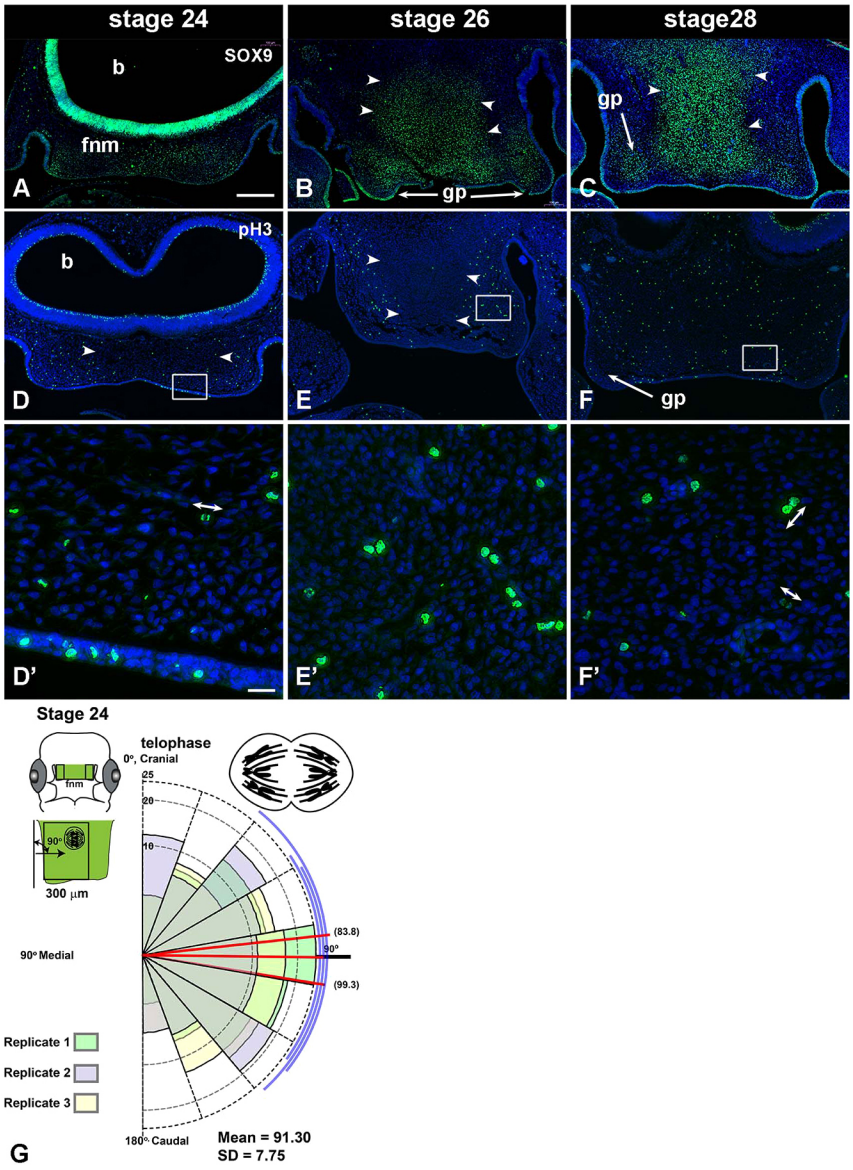

Fig. 2. Mapping chondrogenesis and proliferation in frontonasal mass mesenchyme. (A-C) SOX9 staining marks cells that are fated to become chondrocytes. Staining is increased in non-proliferating regions in the center of the frontonasal mass at stages 26 and 28 (white arrowheads). (D-F′) There are fewer pH3-stained cells in the center (white arrowheads in D,E). (D′,F′). In higher magnification images of the boxed areas in D-F, cells in mitosis or just after cytokinesis are visible (double-headed arrows). (G) The angle of cell division was measured by comparing the axis of cell division to the long axis of the nasal slit (green in schematic). The polar plot shows the angular data from three biological replicates (see coloured fills for replicates 1,2,3). The number of observations are plotted in bins of 20° between 0 and 180°. The means for each biological replicate are shown by red lines. The mean angle of cytokinesis is 91.3° to the cranio-caudal axis. A total of 185 cells were measured across three replicates (approximately 60 nuclei per replicate). Scale bars: 200 µm (A-F); 20 µm (D′-F′). b, brain; fnm, frontonasal mass; gp, globular process.

We next investigated whether the cells themselves were providing shape information. We treated cultures with Y27632, which interferes with Rho and Rac small GTPases (Wei et al., 2001). The Rho family small GTPases, such as Rho, Rac and Cdc42, regulate actomyosin remodeling (Denk-Lobnig and Martin, 2019). We found that the ROCK inhibitor (ROCKi) significantly widened the frontonasal mass by the time the first images were taken (approximately 1 h after inhibitor addition). Then, as the experiment progressed, there was no significant change in width (n=12; Fig. 3E-G). These data suggest that ROCK regulation of the cytoskeleton is essential for normal frontonasal morphogenesis.

We next customized a live-imaging system that would capture the motility of individual frontonasal mesenchymal cells at high resolution. Cultures were grown in Matrigel inside the imaging chamber of an inverted confocal microscope (Fig. 4A,B). Comparisons were made between control and ROCKi-treated cultures after 4.5 h of growth. There was no significant difference in proliferation (Figs S6A, S7A,B) or density (Figs S6B, S7A′,B′). There were also no qualitative differences in the shape of cells (Fig. S7C,D). The ROCKi prevented facial narrowing such that cultures were significantly wider than controls (Fig. S6C). The ROCKi caused no observable increases in apoptosis (Fig. S7E,F); therefore, overall health of the tissue was maintained.

Dynamic cell movements occur in the frontonasal mass mesenchyme and these are regionally coordinated

Having optimized the conditions, a series of live-imaging experiments were carried out (Table 1). A nuclear stain was used to reduce interference from overlapping cell membranes (Fig. 4C-F′; Fig. S7C,D). We tracked hundreds of nuclei across the frontonasal mass at relatively low magnification, thus permitting us to compare cell movement on each side of the face over time (Table 1, Fig. 4C-D′; Movies 1,2). We also collected higher-magnification images next to the nasal slit, a signaling region in the frontonasal mass (Szabo-Rogers et al., 2008) (Fig. 4E-F′, Movies 3,4).

Mathematical analysis of cell tracking data over time and space

To assess all the tracks throughout the experiments, we exported the xy positions at each timepoint from ImageJ and used these

Development (2021) 148, dev193755. doi:10.1242/dev.193755

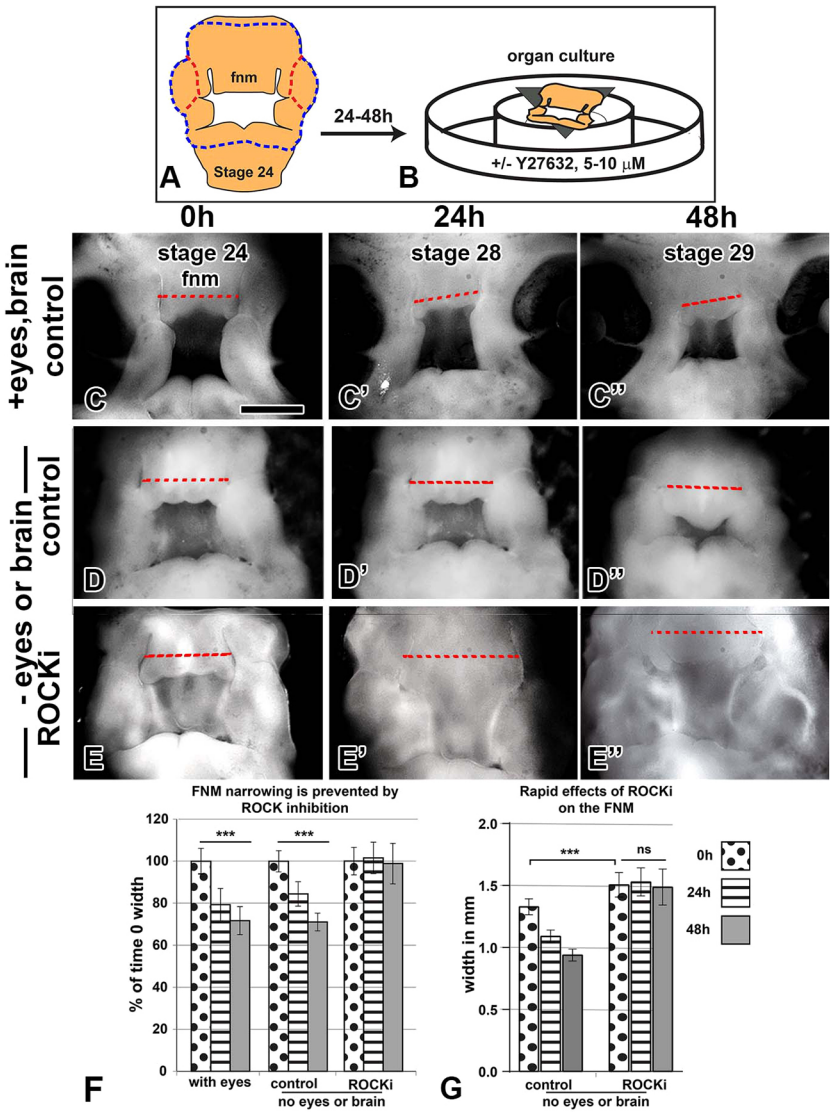

Fig. 3. *In vitro* organ culture of the facial prominences supports morphogenesis. (A,B) Schematic of the organ culture. (A) The blue line outlines the full face plus eyes. The red outline shows the cuts used to remove the eyes. (B) The epithelium is uppermost at the air-liquid interface. (C-E″) Serial images of organ cultures. Facial prominences reached approximately stage 29 after 48 h of culture. (C-D″) Narrowing at the midpoint of the nasal slits (dashed line) occurs with or without the eyes and brain. (E-E″) Cultures treated with either 5 or 10 µM Y27632, have a wider frontonasal mass than controls. (F) Measurements taken across the frontonasal mass (red dashed lines) show that normal cultures decreased in width whereas ROCKi-treated cultures did not. Graph shows width relative to that at time 0 for each condition. (G) Absolute measurements of images collected about 2-4 h after adding ROCKi (time 0 data) show that there is a rapid increase in width of the frontonasal mass. The size of the frontonasal mass does not change between time 0 and 48 h of culture once the ROCKi has been added. ***P<0.001 determined with repeated measures ANOVA and Tukey's post-hoc test (n=12). ns. not significant. Fnm, frontonasal mass. Scale bar: 1 mm.

coordinates for mathematical analyses. First, we quantified the alignment of cell movement directions, S (r,t), across time (Petitjean et al., 2010; Slater et al., 2013). For each time point, t, and radius, r, we found the angle (α_i) between each cell's velocity vector ($\boldsymbol{v_i}$) and the local mean velocity vector ($\boldsymbol{n_i}$) (averaged over a neighborhood of radius r). The neighborhoods were repeated across the frontonasal mass, to cover all the tracks. We then averaged cosine (α_i) over the tissue to obtain S (r,t), and repeated for each r and t (Fig. 4G; see supplementary Materials and Methods).

The degree of alignment of cell movement, S ('order' in Fig. 4H,I; Fig. S8), depends on the direction the cells take relative to their neighbors and the radii of the circular neighborhoods tested. Tissues in which cells move in a similar direction as their neighbors will have S values close to 1, whereas disorganized movement will have S values close to 0 (Fig. 4G). An S~1 is expected for small radii, because cells that are close together have a greater probability of moving in similar directions (Fig. 4G). However, as cell-cell communication decreases over distance, S~0 or disorder is expected for bigger radii (Fig. 4G).

We plotted the order S as a function of time. We found surprising oscillating periods of order and disorder in the control cultures (Fig. 4H-I′; Fig. S8B-D′). During the first 20 min, cultures achieved peak order at S=0.8-0.9 (Fig. 4H,I; Fig. S8B-D). A second peak of order occurred after the first 100 min, followed by a trough 40-50 min later and a recovery in the last hour of the culture period (Fig. 4H; Fig. S8B-D). Surprisingly, the value for S remained at 0.8 or higher for the two periods of order in the control cultures (Fig. 4H′; Fig. S8B′-D′). These fluctuations in order and disorder may be present during normal development of the frontonasal mass. The order (S) decreases as a function of r for three representative time points (Fig. 4H′,I′). In controls, alignment ('ordered movement') can be maintained up to r ~ 150/250 µm. Note that a radius of 200 µm is approximately one-quarter of the frontonasal mass (Fig. 4H, blue line), indicating long-range spatial coordinated cell movement in the controls.

In contrast to the controls, ROCKi-treated samples lacked clear periods of order and disorder throughout the culture period (Fig. 4I; Fig. S8E-G′). In addition, there was a loss of order in radii larger than 50 µm (Fig. 4I′).

K-means clustering analysis reveals regional coordination across the frontonasal mass

In order to visualize the regions of aligned cell movement across the frontonasal mass, we used unbiased k-means clustering. This

Development (2021) 148, dev193755. doi:10.1242/dev.193755

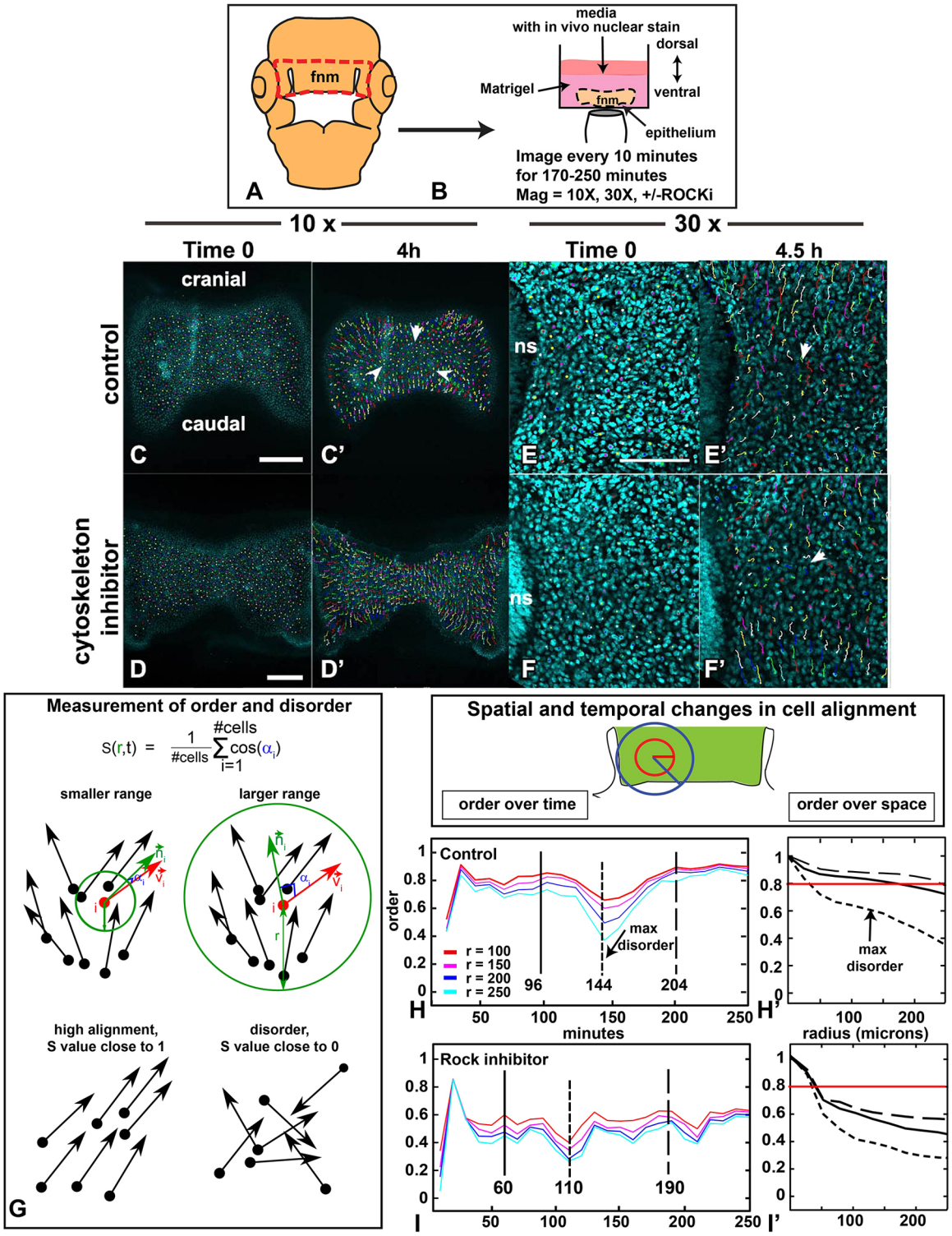

Fig. 4. Manual tracking of cells in the frontonasal mass and calculation of directional order. (A,B) Schematic showing the set-up for live imaging. The red line outlines the area dissected for imaging. The epithelium side is facing down, covered with Matrigel and then media layered on top. (C,C′) The dot is the end of the track and the tail shows all movement of that cell. The tracks in the center of the frontonasal mass appear shorter (white arrowheads, C′). (D,D′) ROCKi was added and the culture spread out relative to controls. After 4 h, the ROCKi culture had not changed in width (D′). (E,E′) The nasal slit is on the left of the images. Tracks appear to be polarized with cranial and caudal tracks moving away from each other. Tracks in the center appear shorter (white arrowhead, E′). (F,F′) The ROCKi culture (10 µM) has shorter tracks (white arrowhead). (G) Directional order, $S(r,t)$, calculated over radius r. Green circles, circular neighborhoods; red arrows, cell velocity (v_i); green arrows, mean direction within neighborhood of radius r (n_i); blue, angle between vectors (α_i). $S(r,t)$=average of cos(α_i) over the tissue at time t. $S(r,t)$ is expected to decrease with increased r. Cells moving in the same direction will have S~1. Random movements, S~0. (H-I′) Vector direction at fixed times was used to determine S as a function of time t. In H′,I′, the solid line is the first peak of order, the short dashed line is the point of maximum disorder, the longer dashed line is the second peak of order. Note that alignment drops for r>200 µm (H′), particularly in ROCKi treatment (I′). Red horizontal line indicates directional order of 0.8. Fnm, frontonasal mass; ns, nasal slit. Red circle is 100 µm in radius and blue circle is 200 µm radius. Scale bars: 250 µm (C-D′);100 µm (in E for E-F′).

Development (2021) 148, dev193755. doi:10.1242/dev.193755

Table 1. Replicates used for live imaging including number of cells tracked in each organ culture and number of time points observed

Organ culture	Number of cells tracked	Number of time points recorded
10×		
C1	638	22
C2	567	25
C3	1040	24
R1	691	26
R2	837	35
R3	706	35
30×		
C4	267	25
C5	43	37
C6	171	37
C7	130	39
C8	187	39
R4	198	40
R5	126	40
R6	145	40

statistical approach clusters data by similarity of a measurement, such as gene expression levels or, in this case, vector direction. We first clustered vectors based on cell position in the frontonasal mass and vector directions (Method 1, testing effects of changing the weight of position, p, or vector, q); see supplementary Materials and Methods). We selected three time points that represent the fluctuation in order and disorder customized to each culture – the first was a time when order was above 0.8, the second when disorder was seen (trough), and the third when order was again above 0.8 (red line in Fig. 4H',I').

We noted that the weight, p (position), q (vector angle), affects the clustering result. With p=0, q=1, clusters appeared spatially diffuse in controls and even more so after ROCKi treatment (Fig. S9A-B″). At the other extreme, p=1, q=0, the tissue was clustered into nine equally shaped rectangular blocks, each one with mixed cell directionality (Fig. S9C-D″). Eventually, we settled on p=2q, for the relative weights as this led to spatially connected clusters of aligned cells (Fig. 5A-A″; Movie 5). The clusters were less coherent in the ROCKi-treated group (Fig. 5B-B″; Movie 6). In the controls, by the end of the experiments, we observed more distinct clustering across the frontonasal mass (Fig. 5A-A″; Fig. S10), suggesting stabilization of coordinated movement. Cell cluster assignment changed over time, as cell directions relative to their neighbors changed over the developmental period (Movie 5). The edges of the clusters of cell vectors (areas where the average direction of the cells differs from neighboring cells) may not form as consistently in the presence of environmental stresses. For example, any stress that affects the cytoskeleton could prevent regional clustering, as we observed with the ROCKi group (Fig. 5B-B″; Movie 6; S10D-F″).

Next, we used local mean directions ($\boldsymbol{n_i}$) over a 200-µm radius neighborhood, which tends to smooth the data and reduce noise from local fluctuations (Method 2, see supplementary Materials and Methods). We chose a neighborhood radius r=200 µm because previous bead implant experiments showed that growth factors or small molecules affect gene expression and proliferation within a range of roughly 200-300 µm away from the bead (Higashihori et al., 2010; Szabo-Rogers et al., 2008), suggesting that cells within r=200 µm could be acting coherently based on the spatial range of tissue signals. Although this motivated our choice of r, lower values of r (e.g. 50, 100 µm) produced similar results using Method 2 (Fig. S11A-D″).

We found that clusters are spatially connected using Method 2 (despite the fact that spatial position is not considered in the clustering) (Fig. 5C-C″; Fig. S12A-C″; Movie 7). There are fewer, more well-defined clustered regions compared with Method (1) weighted on either position or vector direction (roughly six compared with nine). Clustered regions fluctuated more near the beginning and ended with a more stable pattern of clusters towards the end of the cultured time period. Clustering in the disordered state (Fig. 5,C′) is less meaningful, because, based on previous results, we know that cell alignment drops at a radius scale of 50 µm (Fig. 4H′,I′, dashed curve; Fig. S11A-A″). Interestingly, in the controls, cells from the cranial and caudal edges of the frontonasal mass moved in opposite directions (Fig. 5C-C″; Fig. S12C-C″; Movies 5 and 7), correlating with extension in this axis seen *in vivo* (Fig. 1J,M).

ROCKi-treated cultures had more diffuse, disorganized clusters at all time points (Fig. 5D-D″; Fig. S12D-F″; Movie 8). This lack of cell coordination could have been caused by an inability of mesenchymal cells to respond properly to local signaling (including moving or reorienting themselves towards or away from a signal). In addition, the ROCKi treatment disrupted individual cell behaviors.

Our clustering results, especially those for which a radius of 200 µm was imposed, quantify coherent directions of motion in the frontonasal mass.

Right-left symmetry in cell movement is present in the frontonasal mass

The degree of asymmetry is thought to be a readout of developmental instability. For this reason, we measured fluctuating asymmetry over time of individual cell vectors in our samples. The left-side data also serves as a technical replicate of the right side. We first averaged vectors in a 50-µm radius, allowing us to compare the differences at the equivalent grid location (Fig. S13A-D″). There was a high degree of symmetry in the control cultures, particularly in the periods of high order (Fig. 6A,A″). Cells in the left-right portions of the mass appeared to be intermittently coordinating their behavior to maintain symmetry. In states of disorder, there were more asymmetric movements observed (Fig. 6A′,B′; Fig. S14A-C″). This pattern was consistently disrupted in the ROCKi-treated samples in which asymmetry predominated (Fig. 6B-B″; Fig. S14D-F″). Coordination over the extent of this range of 400-500 µm (radii of 200-250 µm) suggests a combination of long-range signaling, cell preprogramming and/or genetic control.

Mapping divergence and convergence within the frontonasal mass

We hypothesized that in order for the frontonasal mass to narrow, there needs to be mediolateral convergence of the cell tracks. In addition, the divergence of cell tracks would be present cranially and caudally based on the geometric morphometrics. We quantified areas of divergence or convergence where vectors were averaged over a 50 µm radius. Grid points were placed every 20 µm in order to make the patterns clearer but averaging was still done at 50 µm. We used a common descriptor of vector-field properties, divergence [div($\boldsymbol{v}$)]. This scalar quantity measures the local tendency of a vector field to point towards or away from each point in space. Given the refined interpolated set of cell velocity vectors (normalized to be unit vectors), we compute the divergence at every point in our grid, and visualize the magnitude as a spatially distributed color field (Fig. 6C-D″; Fig. S15; see supplementary Materials and Methods). Indeed, during high order, vectors generally converged towards the center (Fig. 6C; Fig. S15A-C). During disorder, there were no clear patterns visible (Fig. 6C′; Fig. S15A′-C′), but at the end of the

Development (2021) 148, dev193755. doi:10.1242/dev.193755

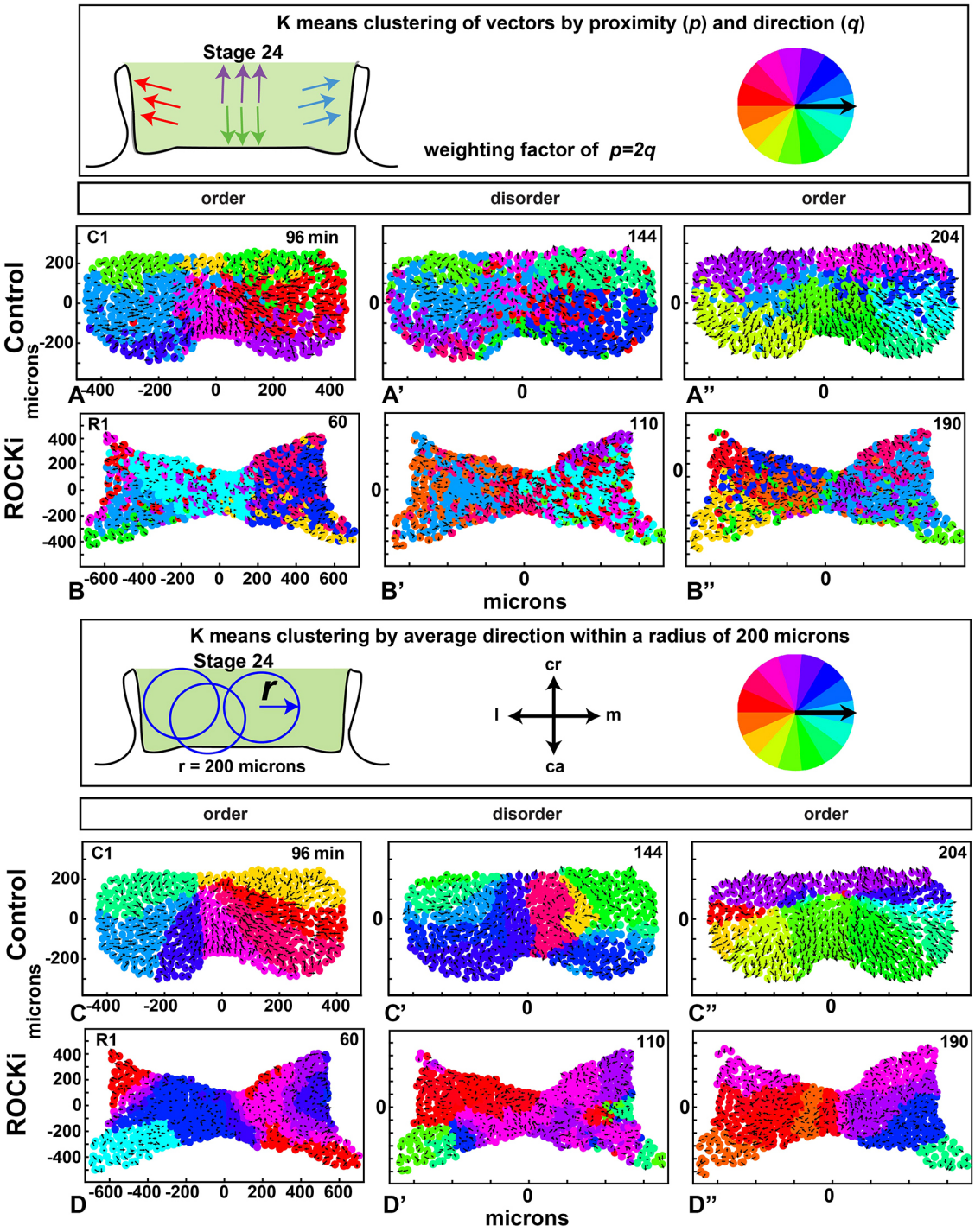

Fig. 5. K-means clustering of vectors. (A-B″) K-means clustering by proximity and direction (Method 1) with relative weights p=2, q=1 at the three time points of high order, disorder and order (as in Fig. 4H,I) for one control (A-A″) and one ROCKi (B-B″) treated culture. (For all data, see Figs S8 and S9.) The black arrows are cell velocity vectors. Color wheel indicates the average direction of each cluster. (C-D″) K-means clustering by average direction within a radius of 200 µm (Method 2). See Movies 5-8. C1, control culture replicate 1; ca, caudal; cr, cranial; l, lateral; m, medial; R1, ROCKi-treated culture replicate 1.

culture, tracks diverged towards the cranial caudal axis (Fig. 6C″; Fig. S15A″-C″; Movie 9). The culture initially exhibited a mediolateral band of divergence between 10-40 min before switching to convergence and then back to divergence at the end. All the control cultures displayed the same pattern (Fig. 8). As predicted from the clustering and symmetry data, ROCKi completely abolished the bands of convergence and divergence (Fig. 6D-D″; Fig. S15D-F″; Movie 10). There were also unpredicted results from the analysis. Based on the tendency for the frontonasal mass to narrow, we expected that cells would converge towards a single vertical line in the cranio-caudal axis. Instead, the cells were gathered towards the center of the frontonasal mass from all corners of the prominence.

To examine local cell behavior further, we carried out analysis on a region close to the nasal slit, a primary source of FGFs at higher magnification. First, we checked whether there were

Development (2021) 148, dev193755. doi:10.1242/dev.193755

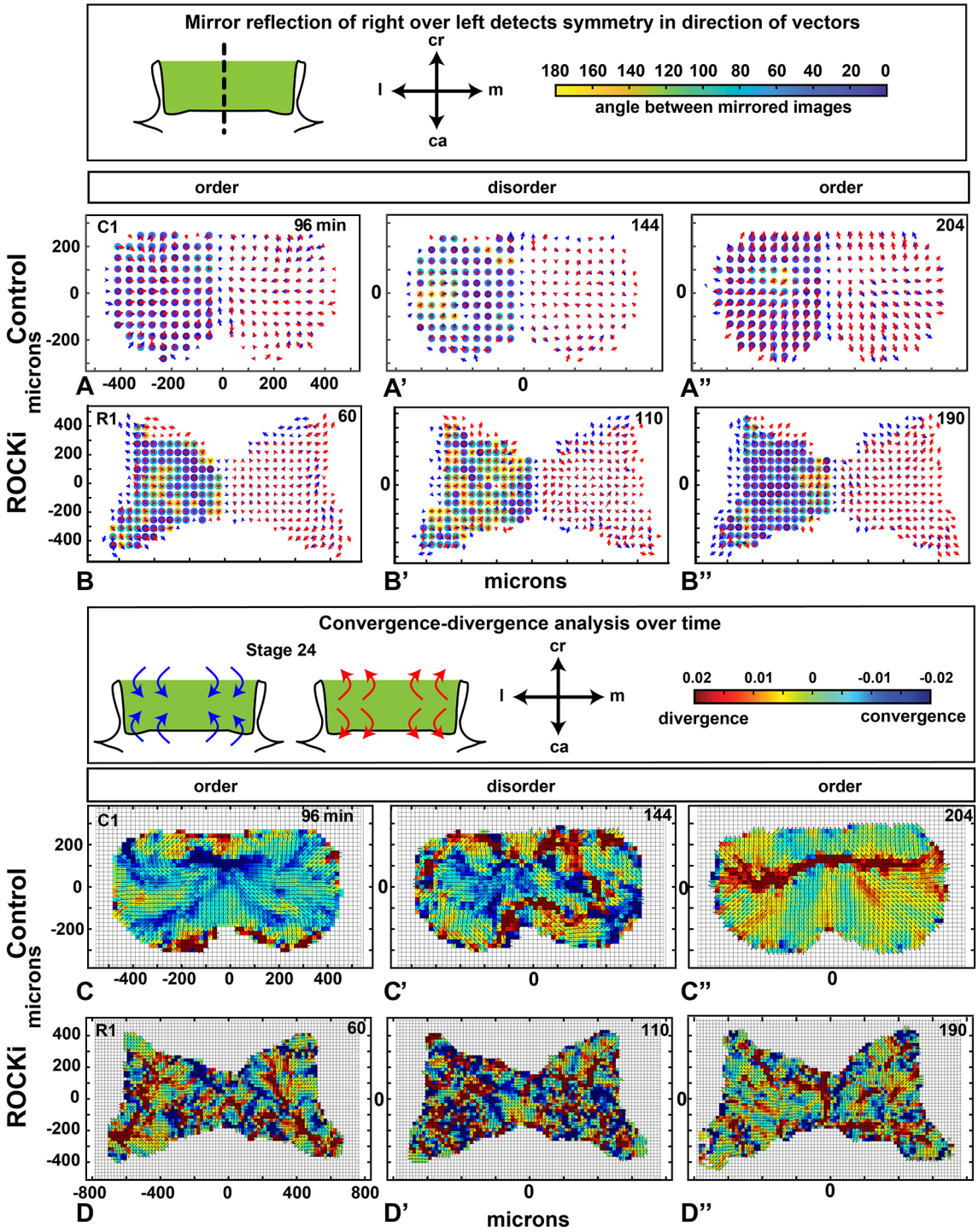

Fig. 6. Right-left symmetry and convergence/divergence are disrupted by ROCKi. Interpolated data (neighborhood averaging of 50 µm) at the three representative times (Fig. 4H,I). (A-B″). (A-A″) High left-right symmetry in ordered states for the control (blue). (B-B″) Clear disruption of symmetry is caused by ROCKi (more yellow). (C-D″) Divergence and convergence (see color scale at the top) across the frontonasal mass. (C-C″) In controls, the first time point had regions of convergence (C). In the disordered state, there were areas of convergence spread across the frontonasal mass (C′). At the end of the cultures, a major band of divergence crossing the frontonasal mass mediolaterally was observed (C″). (D-D″) ROCKi treatment completely disrupted the patterns of convergences and divergence. See Movies 9 and 10. C1, control replicate 1; ca, caudal; cr, cranial; l, lateral; m, medial; R1, ROCKi replicate 1.

periods of order and disorder; however, there were no clear patterns (Fig. S16). Early in the cultures, areas of convergence were sometimes seen close to the nasal slit (Fig. 7A,B,E). The remaining cultures were diverging (Movie 11) between 20 and 50 min (Fig. 7C,D). After 1 h, cultures had mainly a mediolateral band of divergence with several branches similar to those observed at the edges of the 10× data (compare Fig. 6C-C″ imaged at 10× to Fig. 7A′-E′ imaged at 30× magnification). The ROCKi-treated cultures imaged at 30× displayed divergent vectors for the entire culture period with extensive branching (Fig. 7F-H′; Movie 12).

Development (2021) 148, dev193755. doi:10.1242/dev.193755

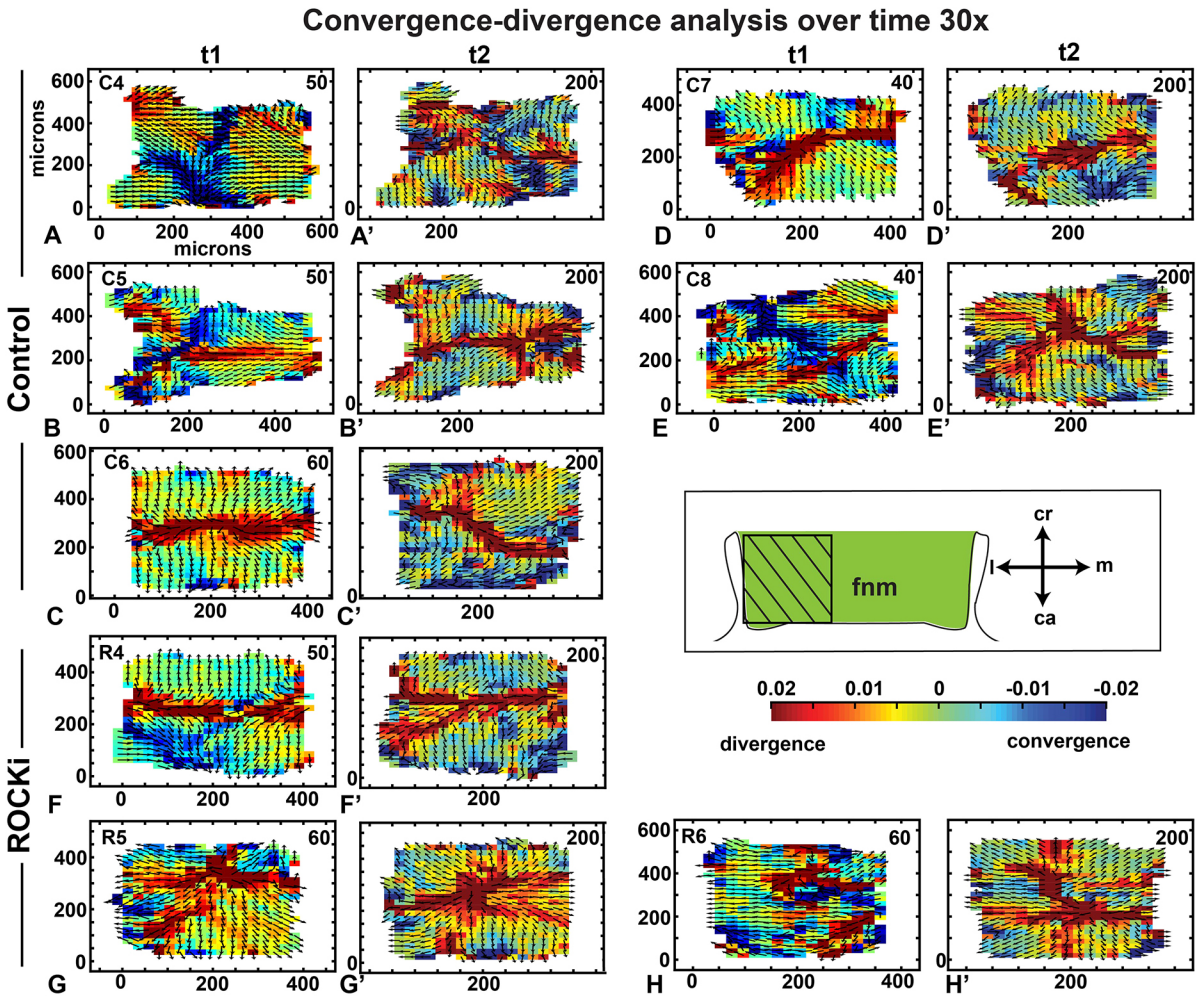

Fig. 7. Convergence-divergence analysis over time at 30× magnification (A-H′) A smaller area of the lateral frontonasal mass was imaged (boxed area in schematic). Nasal slit is to the left. Data were interpolated over a grid of 50 µm. (A-E′) At the first time point, there were cultures with vertical bands of convergence (A,B,E) whereas the other two cultures primarily had divergence patterns (C,D). Bands of divergence were seen in all five control cultures at the later time point (A-E′). (F-H′) The ROCKi cultures showed lines of divergence but with less clear organization. See Movies 11 and 12. C4-8, control replicates 4-8; ca, caudal; cr, cranial; fnm, frontonasal mass; l, lateral; m, medial; R4-6, ROCKi replicates 4-6.

We then used the 30× magnification data to test whether directed cell migration was taking place in the frontonasal mass. The higher resolution imaging was needed to test this hypothesis. The ROCKi caused a decrease in the overall instantaneous speed (Fig. S17A, P=0.009), which may reduce directed cell migration. Indeed, we discovered regional differences in cell behavior, somewhat analogous to the unbiased mathematical clustering (Fig. 5; Figs S9-S12). First, there was relatively less displacement in the center than at the cranial and caudal edges of the frontonasal mass (Fig. S17B; compare regions 4 and 6 with region 5 as shown in the schematic in Fig. S17D). We measured straightness of the cell tracks using the autocorrelation function. Here, cells were more highly directional in the cranial and caudal regions (regions 4 and 6 in the schematic in Fig. S17D) compared with the center (Fig. S17C). The ROCKi decreased displacement (Fig. S17B) but did not appear to interfere with directionality of the cells (Fig. S17C). In point of origin plots, we confirmed that the majority of cranial and caudal cells were diverging from the center (Fig. S17D). There was slightly less polarity to the data from ROCKi-treated cells (Fig. S17E). Thus, ROCKi had the effect of slowing cell movement, especially in the cranial and caudal regions.

Oscillating patterns of convergence-divergence across time

We next wanted to know whether the changes in divergence and convergence patterns correlated with the switch between the order-disorder phases. To answer this, we let the computer algorithm define a band of maximum convergence-divergence and computed the average divergence within that band over time (Fig. 8A-C; see supplementary Materials and Methods). We observed that all control cultures started with a divergence band that lasted for around 60 min of culture, followed by another hour during which a convergent band was observed across the frontonasal mass, and, lastly, a culture period in which the divergent band returned (Fig. 8A-C). Interestingly, this dynamic switching occurred in a 10-20 min time interval, suggesting rapid oscillation between two opposing states. We also observed that dips in order correlate with changes from convergence to divergences (or vice versa). There was more order present when cultures were switching from one direction to the other, a trend seen in all three cultures in the middle of the culture period (Fig. 8A-C).

DISCUSSION

Although we have not yet tested specific cytokines or teratogens in this work, we have identified patterns of movements in cells that are

Development (2021) 148, dev193755. doi:10.1242/dev.193755

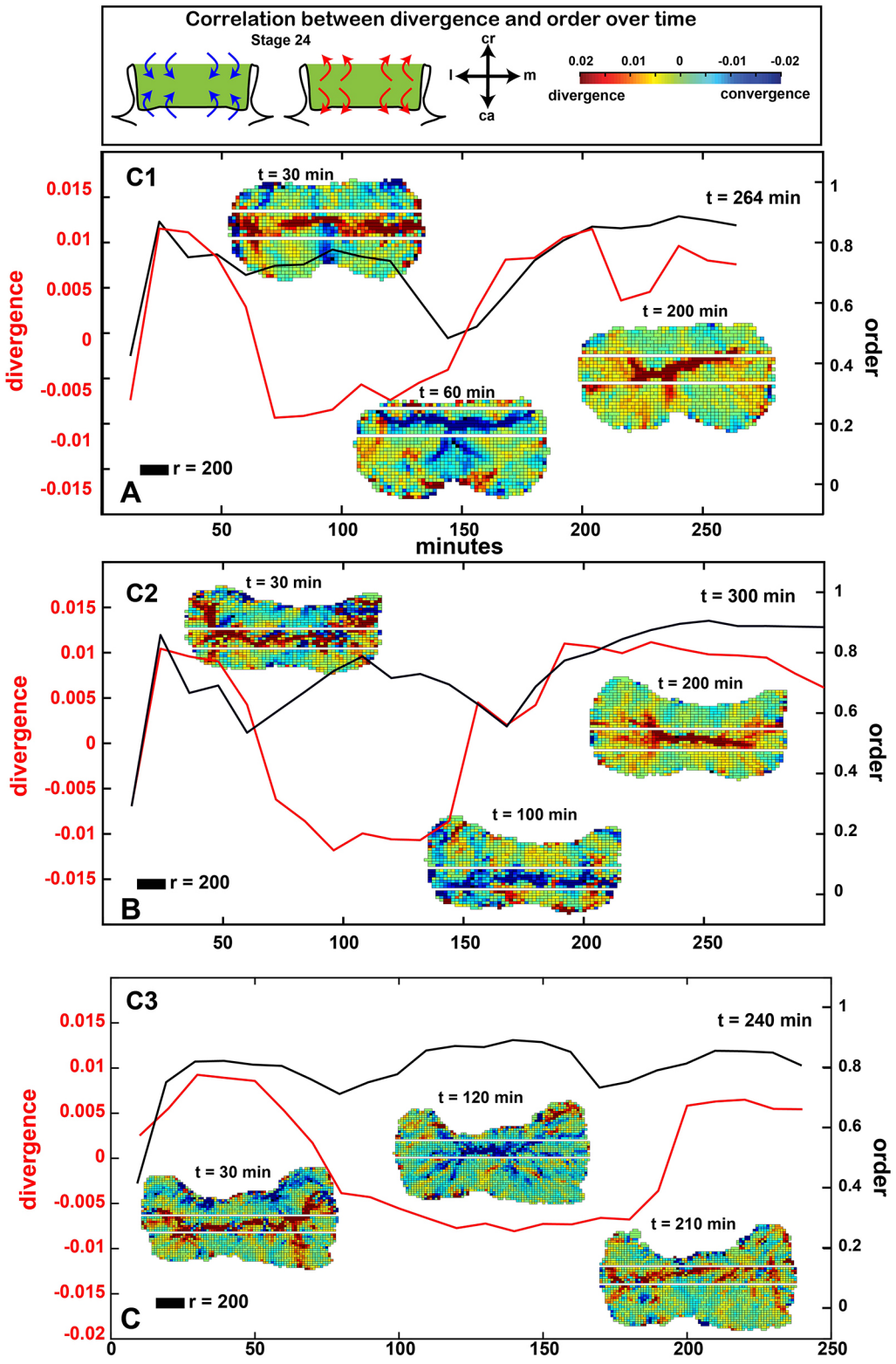

Fig. 8. Oscillations of divergence and order are correlated over time. (A-C) Plots of the fluctuations in divergence and convergence over time in control cultures. The black line reproduces changes in order and disorder (for *r*=200 µm). The red line quantifies the average divergence/convergence computed in the mediolateral band (area between the white lines) covering the grid areas with greatest number of pixels in either red or blue (see supplementary Materials and Methods). All cultures start out with divergence for the first 60-80 min. Then a period of convergence lasts about 100 min before returning to divergence for the end of the culture. The switches between patterns of convergence and divergence are rapid (10-20 min each). See Movie 9. C1-3, control replicates 1-3; ca, caudal; cr, cranial; l, lateral; m, medial.

likely to be affected by multiple signaling pathways. In mouse and chicken experiments, morphogenesis of the frontonasal mass or the midface is regulated by growth factors, such as WNT5A (Kaucka et al., 2017), FGF8 near the nasal slits (Szabo-Rogers et al., 2008), SHH (Marcucio et al., 2015) and BMPs (Ashique et al., 2002; Hu et al., 2015) (Fig. 9). It is possible that FGFs could promote cell movements near the nasal slits, although directional information may not be provided as shown in the limb bud (Gros et al., 2010). BMPs regulate proliferation, lip fusion and patterning as shown by Noggin bead implants (Ashique et al., 2002; Celá et al., 2016). SHH regulates outgrowth of the beak as shown by experiments blocking signaling (Hu et al., 2015). Of all of these networks, the prime candidate for cell movements observed here is the non-canonical, JNK-PCP WNT pathway. The JNK signal results in cytoskeletal

Development (2021) 148, dev193755. doi:10.1242/dev.193755

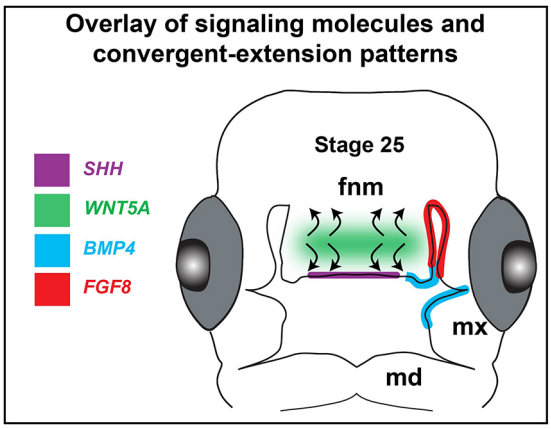

Fig. 9. Overlay of gene expression with patterns of divergence and convergence. Overview of gene expression and proliferation in the frontonasal mass at stage 25. *BMP4*, *SHH* and *FGF8* are expressed in the epithelium whereas *WNT5A* is expressed in the mesenchyme in a medio-lateral band overlapping the region that oscillates between convergence and divergence patterns of cell movements (curved arrows). Fnm, frontonasal mass; md, mandibular prominence; mxp, maxillary prominence.

changes that affect cell shape, orientation, polarity and directed cell migration (Butler and Wallingford, 2017). WNT5A protein induces JNK-PCP signaling activity as shown in facial and limb mesenchyme (Geetha-Loganathan et al., 2014; Gignac et al., 2019; Hosseini-Farahabadi et al., 2013, 2017). *WNT5A* is expressed in a horizontal band across the frontonasal mass at the stages we imaged here (Geetha-Loganathan et al., 2009) (Fig. 9). This band of expression lines up with the computed band of convergent-extension. More direct evidence is needed to determine whether the *WNT5A* signal waxes and wanes; however, we have learned from experiments with the ROCK antagonist that the downstream signaling pathways must be operational in order to see organized fluctuations in cell behavior in the frontonasal mass.

Mouse gene-targeting experiments also support a specific requirement for Rho GTPase signaling in morphogenesis of the midface. Three tissue-specific knockouts of Cdc42 using P0-cre (a neural crest cell cre driver) (Oshima-Nakayama et al., 2016) or Wnt1Cre (neural crest cells) (Fuchs et al., 2009; Liu et al., 2013) or Prrx-Cre (facial mesenchyme) (Aizawa et al., 2012) cause a wide midfacial cleft. *Rac1* was also knocked out conditionally with Wnt1-Cre (Thomas et al., 2010) and a transgene expressing a dominant-negative form of Rho kinase (Phillips et al., 2012) also gave rise to the same phenotype. Rho GTPase signaling is therefore required for midfacial morphogenesis as shown by mouse genetic studies and our chicken cultures treated with a ROCK antagonist.

Oscillation between convergence/divergence, order/disorder and symmetry is evidence of fluctuating asymmetry

Our study yielded several novel results that were not anticipated. We found that the frontonasal mass reaches a stage at which development proceeds independently of signals from the brain and face. This coincides with the time when lip fusion begins. The positions of mesenchymal cells do change in a dynamic fashion across the whole organ and these movements appear to be coordinated over defined regions. In addition, we did not expect that within the imaging period we would encounter some longer cycles, such as the convergent-extension movements that lasted about an hour each (Fig. 8A-C). Underneath these convergent-extension movements there are smaller scale fluctuations as seen with order/disorder, K-means clustering and symmetry. All of these changes in cell behavior are suggestive of an intrinsic developmental instability that exists as part of normal frontonasal mass development. Morphogenesis continues despite the oscillating cell behaviors.

The cell movements that we observed here are on a much smaller scale (estimated to be 2.5 µm over 4 h) than the several millimeters of travel seen in the collective migration of lateral line epithelial cells in the zebrafish or in migrating neural crest cells (Schumacher, 2019). Even though the movements are less than the size of a cell, the mathematical analysis has revealed that they are reproducible across our replicates. Our symmetry analyses are sensitive enough to have ruled out uneven effects of Matrigel on the culture. We have also shown that these cell movements are dependent on GTPase signaling and that blocking this pathway causes a flattening and widening of the culture.

We were surprised to see rapid switching of cell directions from divergence to convergence and back, taking place over a time interval of 10-20 min. These switches in direction were correlated with transitions from order to disorder. In addition, symmetry became weaker during the period of disorder. The biochemical mechanisms are still unclear, but a signal such as Rho GTPase fits the remit. It is well-known that Rho GTPases are prime regulators of the cytoskeleton, forming central hubs in many of the intracellular signaling cascades. Those hubs receive feedback from many sources, whether local (e.g. cell-cell and cell-extracellular matrix adhesion), long-range (chemical signaling via WNT, FGF, etc., or mechanical tension from neighbors or from distant cells pulling on the extracellular matrix). In recent years, a combination of experimental observations and mathematical modeling (Kholodenko, 2006; Park et al., 2017) has demonstrated that the interplay of feedback loops in such signaling networks can give rise to rich sets of dynamics, including cycles of activity, and even spatiotemporal patterns. Disruptions of nodes in such pathways (e.g. the ROCKi inhibition of Rho) can then abrogate or change the wild-type pattern, as we have seen here. In short, the reversal of directions of cells and the break in left-right tissue symmetry is undoubtedly not merely genetically encoded, but also directly dictated by intracellular signaling, shaped by cell-cell interactions in the tissue. A rapid signal such as GEP/GDP is one possible moderator that could be easily susceptible to external stresses leading to such congenital anomalies as cleft lip.

Direction of movement is correlated with anatomical location in the frontonasal mass

We applied a K-means clustering algorithm to identify regions where cells move in the same direction. The maintenance of clear boundaries between neighboring cell populations is required for proper frontonasal development, based on the appearance of control cultures. It does appear that there is a type of coherent repositioning of mesenchymal cells in the face that can be predicted by anatomical location. Certainly, the cranial-caudal divergence from the center was a trend repeated in all the control cultures at all magnifications. However, in ROCKi-treated samples, the clusters of cells were poorly delimited. In treated cultures, there was no evidence of a midline separating the right and left migration patterns. Mapping of clusters of cells will allow us to decipher regional cell responses – genetic and epigenetic – and then ultimately reshaping of the organ during normal and abnormal development.

With these imaging advances, we are seeing the face in a new light, in parallel with other innovations used to see developing embryos in real time (Wallingford, 2019). We first report that cell movements are necessary for frontonasal morphogenesis. Second, an unbiased mathematical clustering of the changes in cell position found surprisingly coordinated and periodic movements that were

Development (2021) 148, dev193755. doi:10.1242/dev.193755

present across an entire organ. Third, the positional changes were largely symmetrical, thus providing the earliest mechanistic understanding of how facial symmetry is established.

Our results represent an overview of the collective cell motility that await the identification of mechanistic causes. Other factors, such as cell elongation, cell-cell or passive movement due to mechanical pulling by other parts of the tissue, may contribute to our findings. In the future, it will be fascinating to see how cell repositioning is affected in the presence of low levels of teratogens. This low-dose experiment will test the extent of buffering capacity in the tissue. If buffering is in place, then coordination and symmetry would be restored when those agents are removed. Finally, we expect that similar types of fluctuating cell behaviors are likely to be present in the other facial prominences and other organs. Our individual cell movement analysis may demonstrate that small fluctuations in cell position are in fact a widespread phenomenon.

MATERIALS AND METHODS

Animals and morphometric analysis of the face

Fertilized white leghorn chicken eggs (*Gallus gallus*) were purchased from the University of Alberta, Edmonton. Eggs were incubated for 3-5 days covering stages 20, 24, 28 and 29 (Hamburger and Hamilton, 1951). Embryos were fixed in 10% formaldehyde and processed into clearing solution for fluorescence-based, optical projection tomography (OPT) as published (Abramyan et al., 2015). Embryos were scanned on a wavelength that excites autofluorescence in formalin-fixed tissues. A total of eight embryos per stage (n=24) were scanned with OPT and reconstructed using NRECON software. Image stacks were visualized using Amira software (FEI v2019.2, Thermo Fisher). Linear measurements were made using the 3D measurement tool, which places marks directly on scanned surfaces. Each frontonasal mass was segmented manually so that volume could be calculated and so that landmarks could be applied on the ventral surfaces facing the brain. Segmented objects were exported as ply files to Landmark and five landmarks were applied as shown in Fig. 1. The landmarks were then exported in NTSYS format to MorphoJ and Procrustes superimposition was carried out. Wireframes were created and discriminant function analysis between two representative stages was carried out in order to visualize the major shape changes in 3D.

Immunofluorescence and TUNEL staining

Paraffin sections were stained with a pH3 antibody (rabbit polyclonal, Cell Signaling Technology, 9701, 1:400), anti SOX9 (Sigma-Aldrich, HPA001758, 1:200), anti Col2A1 (Developmental Studies Hybridoma Bank, CIIC1-b, 1:250) and anti-Myosin II (Developmental Studies Hybridoma Bank, CM1123, 5 µg/ml). Standard antigen retrieval with DIVA Decloaker (BioCare Medical) was carried out. Species-specific secondary antibodies tagged with Alexa Fluor 488 or Cy5 were used (goat anti-mouse 488, A11029; goat anti-rabbit 488, A11034; goat anti-mouse Cy5, A10524, Life Technologies; all at 1:250).

Apoptosis was assessed by TUNEL analysis using the ApopTag Apoptosis Kit (Millipore, S7111) and was detected using fluorescein-tagged anti-digoxygenin antibody as described by Hosseini-Farahabadi et al. (2013). A qualitative assessment of presence of TUNEL-positive cells was carried out.

Nuclei were counterstained in Hoechst 33258 (Sigma-Aldrich, 10 µg/ml in PBS) for 30 min. Slides were mounted with Prolong Gold without DAPI (Invitrogen, P36934). Fluorescence imaging was conducted using a 20× objective on a Panoramic MIDI II slide scanner with 488, Cy5 and DAPI filter sets (3D Histech). High-magnification images were captured with CaseViewer software v.2.4.0.119028 (3D Histech).

Oriented cell division, cell proliferation and cell density analysis

The proportion of cells in metaphase, anaphase, telophase or cytokinesis out of the total number of mitotic figures was determined in frontal and coronal sections. Three biological replicates were counted at stage 24, 26 and 28 in each plane of section. To gather enough cells, the values across four or five sections per animal were summed.

We fixed cultures at 4.5 h after incubation in the microscope chamber and used sections for cell density and proliferation analysis. The total number of $pH3^+$ cells and total number of cells in the frontonasal mass were calculated for one section from each of eight specimens (biological replicates). To estimate total cell number, we used the cell density measurements and calculated the number of cells in the total area of the frontonasal mass. For density, we counted numbers of cells in seven 100 μm^2 areas within each biological replicate. The mean value was calculated for each culture and then this number was used to calculate the average cell density in control and treated cultures. Unpaired, two-tailed, equal variance t-tests were used to compare means in the proliferation and cell density analyses.

Facial organ cultures for static imaging

Chicken eggs were incubated until they reached stage 24-25. In full-face organ cultures, the frontonasal masses including/excluding the eyes and the brain were dissected in 1× Hanks's Balanced Salt Solution with 10% fetal calf serum on ice. The epithelium was left intact for all experiments. Embryonic faces were placed on top of Nucleopore membrane, epithelium side up and the membrane was supported by a wire mesh. Dissections either included all the facial prominences (Fig. 3A, dashed line) or just the frontonasal mass and nasal slits (Fig. 4A, dashed line). Cultures were grown at the air-liquid interface as described (Hu and Helms, 2001). Media was added to each well [900 µl; Dulbecco's Modified Eagle Medium (DMEM)/Ham's F-12, 1:1, with 15 mM HEPES buffer, L-glutamine, 10% fetal bovine serum, 1:100 penicillin/streptomycin/amphotericin B].

We performed a dose-response experiment using 2, 5, 10 or 100 µM ROCK inhibitor (Y27632, Calbiochem, 688000), which is a cell-permeable, highly potent and selective inhibitor of Rho-associated, coiled-coil containing protein kinase (ROCK). We tested a variety of doses as published (Wei et al., 2001) and determined that 10 µM dissolved in DMSO led to detectable changes while not inducing cell death. Lower concentrations had mild effects on cell speed but were too small in magnitude to measure differences in our initial studies. Control cultures were treated with 1 µl of DMSO to 250 µl of media, the same volume used to deliver the ROCKi.

Live imaging of organ cultures

For live imaging, frontonasal mass and lateral nasal prominence explants at stage 25 were transferred to Ibidi microslides (80821, Ibidi) and flipped so that the epithelial surface was contacting the glass. Matrigel (100%, 80 µl, Thermo Fisher) was added on top of the cultures and forceps were used to keep the explant in contact with the dish while the gel set. Media was added to each well (150 µl DMEM:F12 buffered with fresh 20 µM HEPES to equilibrate with room air). This method prevented drift while still allowing 3D morphogenesis to take place. To visualize the nuclei in live cultures, 1 µM Hoechst 33258 was added to the culture media 1 h prior to imaging.

Confocal time-lapse microscopy with 10× and 20× objectives (1.5 zoom on the 20× objective) was carried out (Fig. 4B) using a Leica SP5 inverted confocal microscope with an environmental chamber (37°C) and motorized stage. Image stacks were collected every 10 min for 4-6 h (Table 1). Images were captured at 1024×1024 or 2048×2048 resolution (for 10×), 400 Hz, UV 405 laser (11% power). We imaged ten independent cultures at 10× magnification and six of these were of high enough quality throughout the experiment to be used for manual tracking (Table 1). Another eight cultures were imaged at 30× (Table 1).

Post-processing of images

LIF files produced from Leica software were imported into Fiji (Fiji is ImageJ with additional plugins) using the Bioformats plug-in. Individual organ cultures were separated into stacks and saved as TIF files. Images were edited by using Maximum z Projection on four or five slices of 1 µm thickness in the stack to produce clear images. Images were drift corrected using the Linear Stack Alignment with SIFT plug-in (https://imagej.net/Linear_Stack_Alignment_with_SIFT). The plugin selects multiple points and follows them through the image to correct for drift due to extrinsic forces.

Cell tracking

Two observers, blinded to the experiments, tracked the nuclei. The manual tracking plug-in on Fiji was used to follow nuclei. Dots were placed over the center of the nucleus for each time point. Any nuclei that could not be followed for the entire 24 frames (240 min) were omitted. The entire frontonasal mass was blanketed with tracks at 10×. The tracked images were exported with the options 'Dots & Lines' and 'Overlay Dots' into TIF files. The raw *xy* positional data were used for mathematical clustering and symmetry analysis.

Mathematical analysis of cell tracking data using MatLab

See supplementary Materials and Methods for a detailed description of the mathematical analysis.

Acknowledgements

The authors would like to thank Sevan Hopyan at SickKids hospital in Toronto for a crucial lab visit that inspired the imaging and tracking used in the project. We also thank members of the thesis committee for A.D., Drs Calvin Roskelly, Pamela Hoodless and Clive Roberts at UBC for their guidance.

Competing interests

The authors declare no competing or financial interests.

Author contributions

Conceptualization: A.D., E.G.R., J.M.R.; Methodology: A.D., E.G.R., J.W., K.F., L.E.-K.; Formal analysis: A.D., E.G.R., J.R., J.W., T.A., L.E.-K., J.M.R.; Investigation: A.D., E.G.R.; Data curation: A.D., E.G.R.; Writing - original draft: A.D., E.G.R., J.M.R.; Writing - review & editing: E.G.R., L.E.-K., J.M.R.; Supervision: L.E.-K., J.M.R.; Funding acquisition: J.M.R.

Funding

The work was funded by Canadian Institutes of Health Research (CIHR) project grant (MOP-123536 to J.M.R.). A.D. was funded by a CIHR Canada Graduate Studies Doctoral award and a University of British Columbia 4-year fellowship. E.G.R. and L.E.-K. were funded by a Natural Sciences and Engineering Research Council of Canada Discovery grant (41870 to L.E.-K.). Deposited in PMC for immediate release.

Peer review history

The peer review history is available online at https://journals.biologists.com/dev/article-lookup/doi/10.1242/dev.193755

References

Abramyan, J. and Richman, J. M. (2015). Recent insights into the morphological diversity in the amniote primary and secondary palates. *Dev. Dyn.* **244**, 1457-1468. doi:10.1002/dvdy.24338

Abramyan, J., Thivichon-Prince, B. and Richman, J. M. (2015). Diversity in primary palate ontogeny of amniotes revealed with 3D imaging. *J. Anat.* **226**, 420-433. doi:10.1111/joa.12291

Aizawa, R., Yamada, A., Suzuki, D., Iimura, T., Kassai, H., Harada, T., Tsukasaki, M., Yamamoto, G., Tachikawa, T., Nakao, K. et al. (2012). Cdc42 is required for chondrogenesis and interdigital programmed cell death during limb development. *Mech. Dev.* **129**, 38-50. doi:10.1016/j.mod.2012.02.002

Ashique, A. M., Fu, K. and Richman, J. M. (2002). Endogenous bone morphogenetic proteins regulate outgrowth and epithelial survival during avian lip fusion. *Development* **129**, 4647-4660.

Beames, T. G. and Lipinski, R. J. (2020). Gene-environment interactions: aligning birth defects research with complex etiology. *Development* **147**, dev191064. doi:10.1242/dev.191064

Beaty, T. H., Marazita, M. L. and Leslie, E. J. (2016). Genetic factors influencing risk to orofacial clefts: today's challenges and tomorrow's opportunities. *F1000Res* **5**, 2800. doi:10.12688/f1000research.9503.1

Bénazéraf, B., Beaupeux, M., Tchernookov, M., Wallingford, A., Salisbury, T., Shirtz, A., Shirtz, A., Huss, D., Pourquié, O., François, P. et al. (2017). Multi-scale quantification of tissue behavior during amniote embryo axis elongation. *Development.* **144**, 4462-4472. doi:10.1242/dev.150557

Butler, M. T. and Wallingford, J. B. (2017). Planar cell polarity in development and disease. *Nat. Rev. Mol. Cell Biol.* **18**, 375-388. doi:10.1038/nrm.2017.11

Celá, P., Buchtová, M., Veselá, I., Fu, K., Bogardi, J.-P., Song, Y., Barlow, A., Buxton, P., Medalová, J., Francis-West, P. et al. (2016). BMP signaling regulates the fate of chondro-osteoprogenitor cells in facial mesenchyme in a stage-specific manner. *Dev. Dyn.* **245**:947-962. doi:10.1002/dvdy.24422

Ceuninck, K. and Starbuck, J. M. (2019). A morphometric analysis of developmental instability in children born with unilateral cleft lip and palate. *Clin. Anat.* **32**, 206-211. doi:10.1002/ca.23281

Couly, G. F., Coltey, P. M. and Le Douarin, N. M. (1993). The triple origin of skull in higher vertebrates: a study in quail-chick chimeras. *Development* **117**, 409-429.

Couly, G., Creuzet, S., Bennaceur, S., Vincent, C. and Le Douarin, N. M. (2002). Interactions between Hox-negative cephalic neural crest cells and the foregut endoderm in patterning the facial skeleton in the vertebrate head. *Development* **129**, 1061-1073.

Denk-Lobnig, M. and Martin, A. C. (2019). Modular regulation of Rho family GTPases in development. *Small GTPases* **10**, 122-129. doi:10.1080/21541248.2017.1294234

Diewert, V. M. and Lozanoff, S. (1993). Growth and morphogenesis of the human embryonic midface during primary palate formation analyzed in frontal sections. *J. Craniofac. Genet. Dev. Biol.* **13**, 162-183.

Ekrami, O., Claes, P., White, J. D., Zaidi, A. A., Shriver, M. D. and Van Dongen, S. (2018). Measuring asymmetry from high-density 3D surface scans: an application to human faces. *PLoS ONE* **13**, e0207895. doi:10.1371/journal.pone.0207895

Ekrami, O., Claes, P., White, J. D., Weinberg, S. M., Marazita, M. L., Walsh, S., Shriver, M. D. and Van Dongen, S. (2020). A multivariate approach to determine the dimensionality of human facial asymmetry. *Symmetry-Basel* **12**, 348. doi:10.3390/sym12030348

Everson, J. L., Fink, D. M., Yoon, J. W., Leslie, E. J., Kietzman, H. W., Ansen-Wilson, L. J., Chung, H. M., Walterhouse, D. O., Marazita, M. L. and Lipinski, R. J. (2017). Sonic hedgehog regulation of Foxf2 promotes cranial neural crest mesenchyme proliferation and is disrupted in cleft lip morphogenesis. *Development* **144**, 2082-2091. doi:10.1242/dev.149930

Ferretti, E., Li, B., Zewdu, R., Wells, V., Hebert, J. M., Karner, C., Anderson, M. J., Williams, T., Dixon, J., Dixon, M. J. et al. (2011). A conserved Pbx-Wnt-p63-Irf6 regulatory module controls face morphogenesis by promoting epithelial apoptosis. *Dev. Cell* **21**, 627-641. doi:10.1016/j.devcel.2011.08.005

Fuchs, S., Herzog, D., Sumara, G., Büchmann-Møller, S., Civenni, G., Wu, X., Chrostek-Grashoff, A., Suter, U., Ricci, R., Relvas, J. B. et al. (2009). Stage-specific control of neural crest stem cell proliferation by the small rho GTPases Cdc42 and Rac1. *Cell Stem Cell* **4**, 236-247. doi:10.1016/j.stem.2009.01.017

Geetha-Loganathan, P., Nimmagadda, S., Antoni, L., Fu, K., Whiting, C. J., Francis-West, P. and Richman, J. M. (2009). Expression of WNT signalling pathway genes during chicken craniofacial development. *Dev. Dyn.* **238**, 1150-1165. doi:10.1002/dvdy.21934

Geetha-Loganathan, P., Nimmagadda, S., Fu, K. and Richman, J. M. (2014). Avian facial morphogenesis is regulated by c-Jun N-terminal kinase/planar cell polarity (JNK/PCP) wingless-related (WNT) signaling. *J. Biol. Chem.* **289**, 24153-24167. doi:10.1074/jbc.M113.522003

Gignac, S. J., Hosseini-Farahabadi, S., Akazawa, T., Schuck, N. J., Fu, K. and Richman, J. M. (2019). Robinow syndrome skeletal phenotypes caused by the WNT5AC83S variant are due to dominant interference with chondrogenesis. *Hum. Mol. Genet.* **28**, 2395-2414. doi:10.1093/hmg/ddz071

Gros, J., Hu, J. K.-H., Vinegoni, C., Feruglio, P. F., Weissleder, R. and Tabin, C. J. (2010). WNT5A/JNK and FGF/MAPK pathways regulate the cellular events shaping the vertebrate limb bud. *Curr. Biol.* **20**, 1993-2002. doi:10.1016/j.cub.2010.09.063

Grosen, D., Bille, C., Petersen, I., Skytthe, A., Hjelmborg, J. B., Pedersen, J. K., Murray, J. C. and Christensen, K. (2011). Risk of oral clefts in twins. *Epidemiology* **22**, 313-319. doi:10.1097/EDE.0b013e3182125f9c

Gundlach, K. K. H. and Maus, C. (2006). Epidemiological studies on the frequency of clefts in Europe and world-wide. *J. Craniomaxillofac. Surg.* **34** Suppl. 2, 1-2. doi:10.1016/S1010-5182(06)60001-2

Hamburger, V. and Hamilton, H. L. (1951). A series of normal stages in the development of the chick embryo. *J. Morphol.* **88**, 49-92. doi:10.1002/jmor.1050880104

Higashihori, N., Buchtová, M. and Richman, J. M. (2010). The function and regulation of TBX22 in avian frontonasal morphogenesis. *Dev. Dyn.* **239**, 458-473. doi:10.1002/dvdy.22182

Hosseini-Farahabadi, S., Geetha-Loganathan, P., Fu, K., Nimmagadda, S., Yang, H. J. and Richman, J. M. (2013). Dual functions for WNT5A during cartilage development and in disease. *Matrix Biol.* **32**, 252-264. doi:10.1016/j.matbio.2013.02.005

Hosseini-Farahabadi, S., Gignac, S. J., Danescu, A., Fu, K. and Richman, J. M. (2017). Abnormal WNT5A signaling causes mandibular hypoplasia in Robinow syndrome. *J. Dent. Res.* **96**, 1265-1272. doi:10.1177/0022034517716916

Hu, D. and Helms, J. (2001). Organ culture of craniofacial primordia. *Methods* **24**, 49-54. doi:10.1006/meth.2001.1156

Hu, D. and Marcucio, R. S. (2009a). A SHH-responsive signaling center in the forebrain regulates craniofacial morphogenesis via the facial ectoderm. *Development* **136**, 107-116. doi:10.1242/dev.026583

Hu, D. and Marcucio, R. S. (2009b). Unique organization of the frontonasal ectodermal zone in birds and mammals. *Dev. Biol.* **325**, 200-210. doi:10.1016/j.ydbio.2008.10.026

Hu, D., Marcucio, R. S. and Helms, J. A. (2003). A zone of frontonasal ectoderm regulates patterning and growth in the face. *Development* **130**, 1749-1758. doi:10.1242/dev.00397

Hu, D., Young, N. M., Li, X., Xu, Y., Hallgrimsson, B. and Marcucio, R. S. (2015). A dynamic Shh expression pattern, regulated by SHH and BMP signaling, coordinates fusion of primordia in the amniote face. *Development* **142**, 567-574. doi:10.1242/dev.114835

Jin, Y.-R., Han, X. H., Taketo, M. M. and Yoon, J. K. (2012). Wnt9b-dependent FGF signaling is crucial for outgrowth of the nasal and maxillary processes during upper jaw and lip development. *Development* **139**, 1821-1830. doi:10.1242/dev.075796

Juriloff, D. M. and Harris, M. J. (2008). Mouse genetic models of cleft lip with or without cleft palate. *Birth Defects Res. A Clin. Mol. Teratol* **82**, 63-77. doi:10.1002/bdra.20430

Katsube, M., Rolfe, S. M., Bortolussi, S. R., Yamaguchi, Y., Richman, J. M., Yamada, S. and Vora, S. R. (2019). Analysis of facial skeletal asymmetry during foetal development using μCT imaging. *Orthod. Craniofac. Res.* **22** Suppl. 1, 199-206. doi:10.1111/ocr.12304

Kaucka, M., Ivashkin, E., Gyllborg, D., Zikmund, T., Tesarova, M., Kaiser, J., Xie, M., Petersen, J., Pachnis, V., Nicolis, S. K. et al. (2016). Analysis of neural crest-derived clones reveals novel aspects of facial development. *Sci. Adv.* **2**, e1600060. doi:10.1126/sciadv.1600060

Kaucka, M., Zikmund, T., Tesarova, M., Gyllborg, D., Hellander, A., Jaros, J., Kaiser, J., Petersen, J., Szarowska, B., Newton, P. T. et al. (2017). Oriented clonal cell dynamics enables accurate growth and shaping of vertebrate cartilage. *eLife* **6**, e25902. doi:10.7554/eLife.25902

Kholodenko, B. N. (2006). Cell-signalling dynamics in time and space. *Nat. Rev. Mol. Cell Biol.* **7**, 165-176. doi:10.1038/nrm1838

Klingenberg, C. P. (2011). Morphoj: An integrated software package for geometric morphometrics. *Mol. Ecol. Resour.* **11**, 353-357. doi:10.1111/j.1755-0998.2010.02924.x

Kulesa, P. M., Bailey, C. M., Cooper, C. and Fraser, S. E. (2010). In ovo live imaging of avian embryos. *Cold Spring Harb. Protoc.* **2010**, pdb prot5446. doi:10.1101/pdb.prot5446

Lee, S.-H., Bédard, O., Buchtová, M., Fu, K. and Richman, J. M. (2004). A new origin for the maxillary jaw. *Dev. Biol.* **276**, 207-224. doi:10.1016/j.ydbio.2004.08.045

Leslie, E. J. and Marazita, M. L. (2013). Genetics of cleft lip and cleft palate. *Am. J. Med. Genet. C Semin. Med. Genet.* **163**, 246-258. doi:10.1002/ajmg.c.31381

Leslie, E. J., Carlson, J. C., Cooper, M. E., Christensen, K., Weinberg, S. M. and Marazita, M. L. (2017). Exploring subclinical phenotypic features in twin pairs discordant for cleft lip and palate. *Cleft Palate Craniofac. J.* **54**, 90-93. doi:10.1597/15-190

Liu, Y., Jin, Y., Li, J., Seto, E., Kuo, E., Yu, W., Schwartz, R. J., Blazo, M., Zhang, S. L. and Peng, X. (2013). Inactivation of Cdc42 in neural crest cells causes craniofacial and cardiovascular morphogenesis defects. *Dev. Biol.* **383**, 239-252. doi:10.1016/j.ydbio.2013.09.013

Losa, M., Risolino, M., Li, B., Hart, J., Quintana, L., Grishina, I., Yang, H., Choi, I. F., Lewicki, P., Khan, S. et al. (2018). Face morphogenesis is promoted by Pbx-dependent EMT via regulation of Snail1 during frontonasal prominence fusion. *Development* **145**, dev157628. doi:10.1242/dev.157628

Ludwig, K. U., Bohmer, A. C., Bowes, J., Nikolić, M., Ishorst, N., Wyatt, N., Hammond, N. L., Gölz, L., Thieme, F., Barth, S. et al. (2017). Imputation of orofacial clefting data identifies novel risk loci and sheds light on the genetic background of cleft lip±cleft palate and cleft palate only. *Hum. Mol. Genet.* **26**, 829-842. doi:10.1093/hmg/ddx012

Marcucio, R., Hallgrimsson, B. and Young, N. M. (2015). Facial morphogenesis: physical and molecular interactions between the brain and the face. *Curr. Top. Dev. Biol.* **115**, 299-320. doi:10.1016/bs.ctdb.2015.09.001

McColl, J., Mok, G. F., Lippert, A. H., Ponjavic, A., Muresan, L. and Münsterberg, A. (2018). 4D imaging reveals stage dependent random and directed cell motion during somite morphogenesis. *Sci. Rep.* **8**, 12644. doi:10.1038/s41598-018-31014-3

McGonnell, I. M., Clarke, J. D. W. and Tickle, C. (1998). Fate map of the developing chick face: Analysis of expansion of facial primordia and establishment of the primary palate. *Dev. Dyn.* **212**, 102-118. doi:10.1002/(SICI)1097-0177(199805)212:1<102::AID-AJA10>3.0.CO;2-9

Noden, D. M. (1978). The control of avian cephalic neural crest cytodifferentiation: I. Skeletal and connective tissues. *Dev. Biol.* **67**, 296-312. doi:10.1016/0012-1606(78)90201-4

O'Rahilly, R. and Müller, F. (2007). The development of the neural crest in the human. *J. Anat.* **211**, 335-351. doi:10.1111/j.1469-7580.2007.00773.x

Oshima-Nakayama, M., Yamada, A., Kurosawa, T., Aizawa, R., Suzuki, D., Saito, Y., Kassai, H., Sato, Y., Yamamoto, M., Shirota, T. et al. (2016). Cdc42 is crucial for facial and palatal formation during craniofacial development. *Bone Rep.* **5**, 1-6. doi:10.1016/j.bonr.2016.01.001

Park, J. S., Holmes, W. R., Lee, S. H., Kim, H.-N., Kim, D.-H., Kwak, M. K., Wang, C. J., Edelstein-Keshet, L. and Levchenko, A. (2017). Mechanochemical feedback underlies coexistence of qualitatively distinct cell polarity patterns within diverse cell populations. *Proc. Natl. Acad. Sci. USA* **114**, E5750-E5759. doi:10.1073/pnas.1700054114

Parsons, T. E., Kristensen, E., Hornung, L., Diewert, V. M., Boyd, S. K., German, R. Z. and Hallgrímsson, B. (2008). Phenotypic variability and craniofacial dysmorphology: Increased shape variance in a mouse model for cleft lip. *J. Anat.* **212**, 135-143. doi:10.1111/j.1469-7580.2007.00845.x

Patterson, S. B., Johnston, M. C. and Minkoff, R. (1984). An implant labeling technique employing sable hair probes as carriers for 3H-thymidine: Applications to the study of facial morphogenesis. *Anat. Rec.* **210**, 525-536. doi:10.1002/ar.1092100313

Petitjean, L., Reffay, M., Grasland-Mongrain, E., Poujade, M., Ladoux, B., Buguin, A. and Silberzan, P. (2010). Velocity fields in a collectively migrating epithelium. *Biophys. J.* **98**, 1790-1800. doi:10.1016/j.bpj.2010.01.030

Phillips, H. M., Papoutsi, T., Soenen, H., Ybot-Gonzalez, P., Henderson, D. J. and Chaudhry, B. (2012). Neural crest cell survival is dependent on rho kinase and is required for development of the mid face in mouse embryos. *PLoS ONE* **7**, e37685. doi:10.1371/journal.pone.0037685

Richman, J. M. and Tickle, C. (1989). Epithelia are interchangeable between facial primordia of chick embryos and morphogenesis is controlled by the mesenchyme. *Dev. Biol.* **136**, 201-210. doi:10.1016/0012-1606(89)90142-5

Richman, J. M. and Vora, S. R. (2017). *Craniofacial Defects and Cleft Lip and Palate. Encyclopedia of Life Sciences*. Wiley. doi:10.1002/9780470015902.a0020915.pub2

Richmond, S., Howe, L. J., Lewis, S., Stergiakouli, E. and Zhurov, A. (2018). Facial genetics: a brief overview. *Front. Genet.* **9**, 462. doi:10.3389/fgene.2018.00462

Roosenboom, J., Indencleef, K., Hens, G., Peeters, H., Christensen, K., Marazita, M. L., Claes, P., Leslie, E. J. and Weinberg, S. M. (2017). Testing the face shape hypothesis in twins discordant for nonsyndromic orofacial clefting. *Am. J. Med. Genet. A* **173**, 2886-2892. doi:10.1002/ajmg.a.38471

Schneider, R. A. (2018). Neural crest and the origin of species-specific pattern. *Genesis* **56**, e23219. doi:10.1002/dvg.23219

Schneider, R. A. and Helms, J. A. (2003). The cellular and molecular origins of beak morphology. *Science* **299**, 565-568. doi:10.1126/science.1077827

Schumacher, L. (2019). Collective cell migration in development. *Adv. Exp. Med. Biol.* **1146**, 105-116. doi:10.1007/978-3-030-17593-1_7

Slater, B., Londono, C. and McGuigan, A. P. (2013). An algorithm to quantify correlated collective cell migration behavior. *BioTechniques* **54**, 87-92. doi:10.2144/000113990

Song, L., Li, Y., Wang, K., Wang, Y.-Z., Molotkov, A., Gao, L., Zhao, T., Yamagami, T., Wang, Y., Gan, Q. et al. (2009). Lrp6-mediated canonical Wnt signaling is required for lip formation and fusion. *Development* **136**, 3161-3171. doi:10.1242/dev.037440

Szabo-Rogers, H. L., Geetha-Loganathan, P., Nimmagadda, S., Fu, K. K. and Richman, J. M. (2008). FGF signals from the nasal pit are necessary for normal facial morphogenesis. *Dev. Biol.* **318**, 289-302. doi:10.1016/j.ydbio.2008.03.027

Tao, H., Zhu, M., Lau, K., Whitley, O. K. W., Samani, M., Xiao, X., Chen, X. X., Hahn, N. A., Liu, W., Valencia, M. et al. (2019). Oscillatory cortical forces promote three dimensional cell intercalations that shape the murine mandibular arch. *Nat. Commun.* **10**, 1703. doi:10.1038/s41467-019-09540-z

Thomas, P. S., Kim, J., Nunez, S., Glogauer, M. and Kaartinen, V. (2010). Neural crest cell-specific deletion of Rac1 results in defective cell-matrix interactions and severe craniofacial and cardiovascular malformations. *Dev. Biol.* **340**, 613-625. doi:10.1016/j.ydbio.2010.02.021

Thornhill, R. and Møller, A. P. (1997). Developmental stability, disease and medicine. *Biol. Rev.* **72**, 497-548. doi:10.1017/S0006323197005082

Van Dongen, S. (2007). What do we know about the heritability of developmental instability? Answers from a Bayesian model. *Evolution* **61**, 1033-1042. doi:10.1111/j.1558-5646.2007.00096.x

Vega-Lopez, G. A., Cerrizuela, S., Tribulo, C. and Aybar, M. J. (2018). Neurocristopathies: New insights 150 years after the neural crest discovery. *Dev. Biol.* **444** Suppl. 1, S110-S143. doi:10.1016/j.ydbio.2018.05.013

Voiculescu, O., Bertocchini, F., Wolpert, L., Keller, R. E. and Stern, C. D. (2007). The amniote primitive streak is defined by epithelial cell intercalation before gastrulation. *Nature* **449**, 1049-1052. doi:10.1038/nature06211

Wallingford, J. B. (2019). The 200-year effort to see the embryo. *Science* **365**, 758-759. doi:10.1126/science.aaw7565

Wang, K. Y., Juriloff, D. M. and Diewert, V. M. (1995). Deficient and delayed primary palatal fusion and mesenchymal bridge formation in cleft lip-liable strains of mice. *J. Craniofac. Genet. Dev. Biol.* **15**, 99-116.

Wei, L., Roberts, W., Wang, L., Yamada, M., Zhang, S., Zhao, Z., Rivkees, S. A., Schwartz, R. J. and Imanaka-Yoshida, K. (2001). Rho kinases play an obligatory role in vertebrate embryonic organogenesis. *Development* **128**, 2953-2962.

Weinberg, S. M., Naidoo, S. D., Bardi, K. M., Brandon, C. A., Neiswanger, K., Resick, J. M., Martin, R. A. and Marazita, M. L. (2009). Face shape of unaffected parents with cleft affected offspring: combining three-dimensional surface imaging

and geometric morphometrics. *Orthod. Craniofac. Res.* **12**, 271-281. doi:10.1111/j.1601-6343.2009.01462.x

Wu, P., Jiang, T.-X., Shen, J.-Y., Widelitz, R. B. and Chuong, C.-M. (2006). Morphoregulation of avian beaks: Comparative mapping of growth zone activities and morphological evolution. *Dev. Dyn.* **235**, 1400-1412. doi:10.1002/dvdy.20825

Young, N. M., Chong, H. J., Hu, D., Hallgrimsson, B. and Marcucio, R. S. (2010). Quantitative analyses link modulation of sonic hedgehog signaling to continuous variation in facial growth and shape. *Development* **137**, 3405-3409. doi:10.1242/dev.052340

Zhang, C., Miller, S. F., Roosenboom, J., Wehby, G. L., Moreno Uribe, L. M., Hecht, J. T., Deleyiannis, F. W. B., Christensen, K., Marazita, M. L. and Weinberg, S. M. (2018). Soft tissue nasal asymmetry as an indicator of orofacial cleft predisposition. *Am. J. Med. Genet. A* **176**, 1296-1303. doi:10.1002/ajmg.a.38688

Supplementary Figures

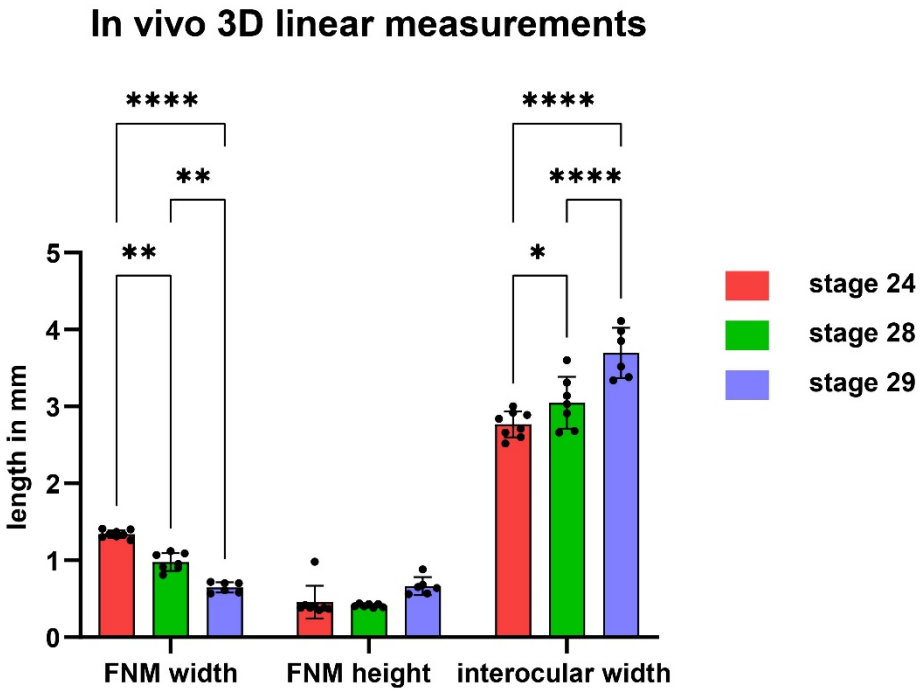

Figure S1. 3D linear measurements from reconstructed OPT scans of chicken embryo heads. Scans were imported into Amira software for visualization and measurements. Frontonasal mass width was measured at the midpoint between the cranial and caudal edges of the nasal slit. Frontonasal mass height was measured in the midline from a line connecting the top of the nasal slits to the caudal tip of the frontonsal mass. Interocular width was measured through the head between the two eyes. Significant decreases in absolute frontonasal mass width occurred between all stages. No significant increase in frontonasal mass height was detected however interocular with increased by approximately 38% when comparing stage 24 and 29. Thus the overall head size increases while the midface narrows. The frontonasal mass width values correspond very closely to the organ cultures started at stage 24 and grown for 48h (Fig. 3G). Key: FNM – frontonasal mass

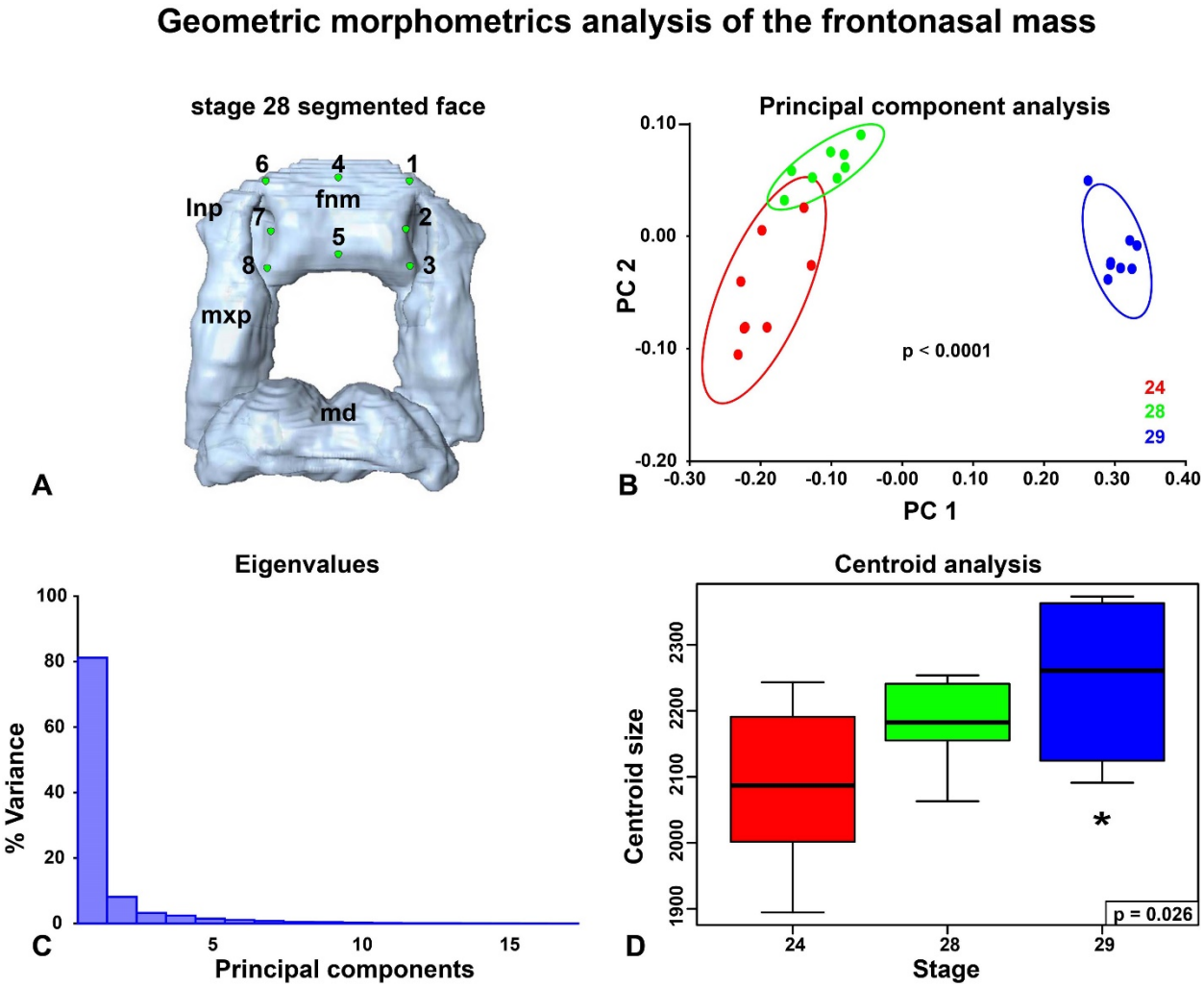

Figure S2. 3D Geometric Morphometrics analysis of the frontonasal mass at 3 stages of development. **A)** Placement of landmarks on a segmented face. By isolated the face from the head we were able to capture the thickness of the frontonasal mass with landmarks 1,6,7 and 8. B) The PC analysis revealed significant separation based on shape between stage 24 ,28 and 29 frontonasal mass. The low P value is due to the stage 29 shape being so different than the younger stages. C) The majority of the variance (more than 80%) is captured in PC1 which probably captures the extension of the cranial-caudal axis. D) The centroid sizes are similar at stage 24 and 28 but significantly larger in stage 29 embryos. Landmarks are more spread out at stage 29 which relates to increased growth. P value determined with Tukey's post hoc test for multiple comparisons.

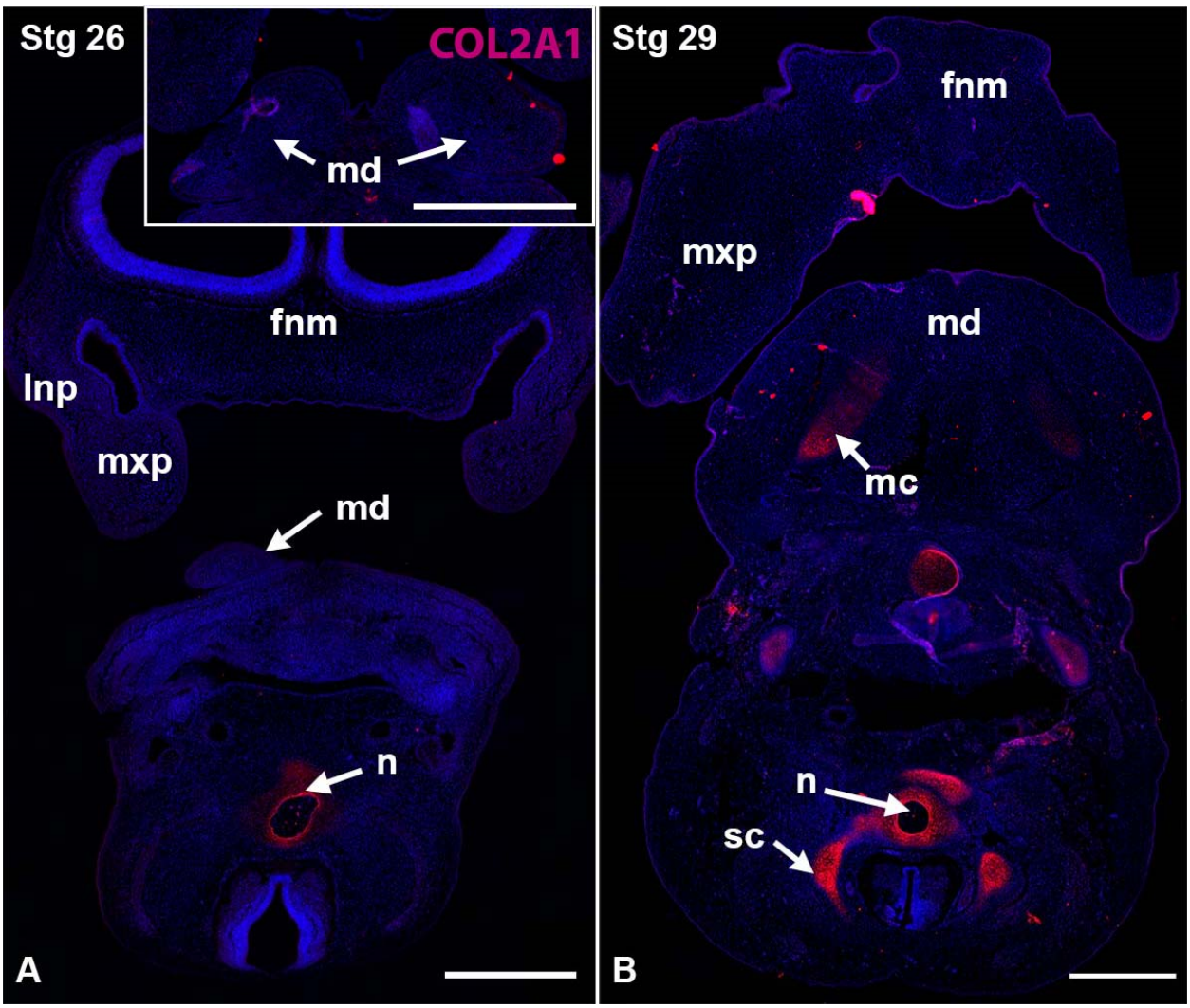

Figure S3. Immunostaining of the head of chicken embryos. Frontal sections cut through the frontonasal mass and mandible. A) At stage 26, midway between stage 24 and 28, there is no expression of COL2A1 (type II collagen) in the frontonasal mass or mandibular prominence (inset). The inset has some folds in the tissue but there is no signal for COL2A1. The only expression is seen in the notochord and surrounding mesenchyme. B) at stage 29 there is expression detected in Meckel's cartilage of the mandible, however there is no staining in the frontonasal mass. The mandible is differentiating prior to the frontonasal mass.
Key: fnm – frontonasal mass, lnp – lateral nasal prominence, mc – Meckel's cartilage, md – mandibular prominence, n – notochord, sc – sclerotome. Scale bar = 500 microns.

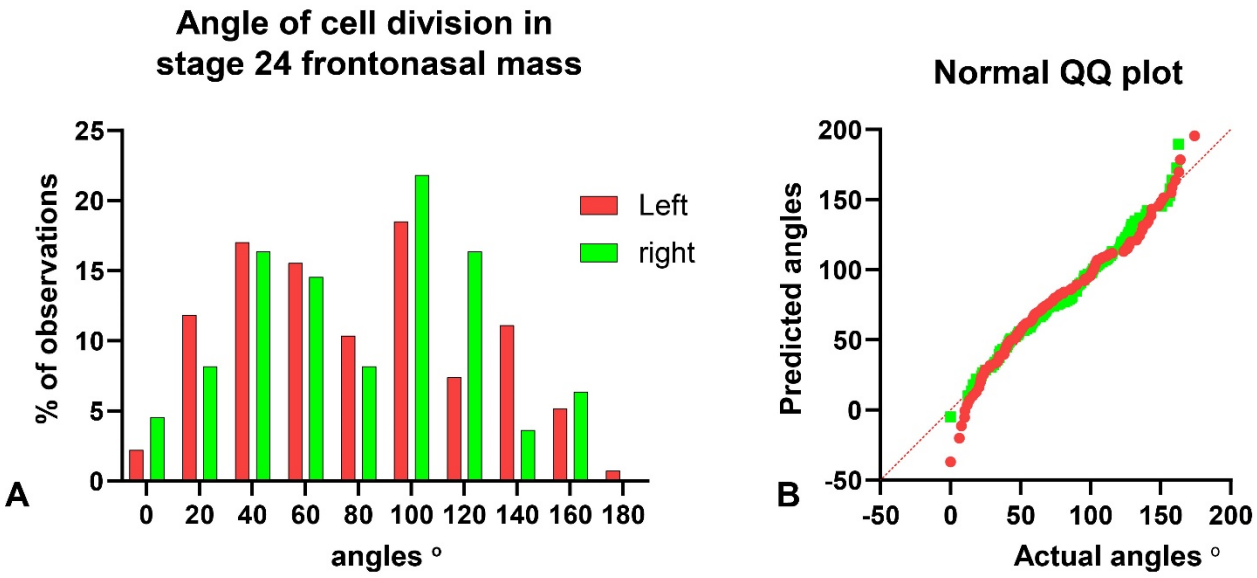

Figure S4. Frequency of observations of the angle of cell division when cells are in telophase. Cells were stained with pH3 antibody and angle of division was measured relative to the nasal slit. Zero and 180 degrees are parallel to the nasal slit. A) The observations in the left and right side are plotted separately. Generally there is no difference in the proportions of observations seen in the R and L sides. The exceptions are at 120 and 140 degrees. B) The overall normality of the data is not significantly different from predicted values.

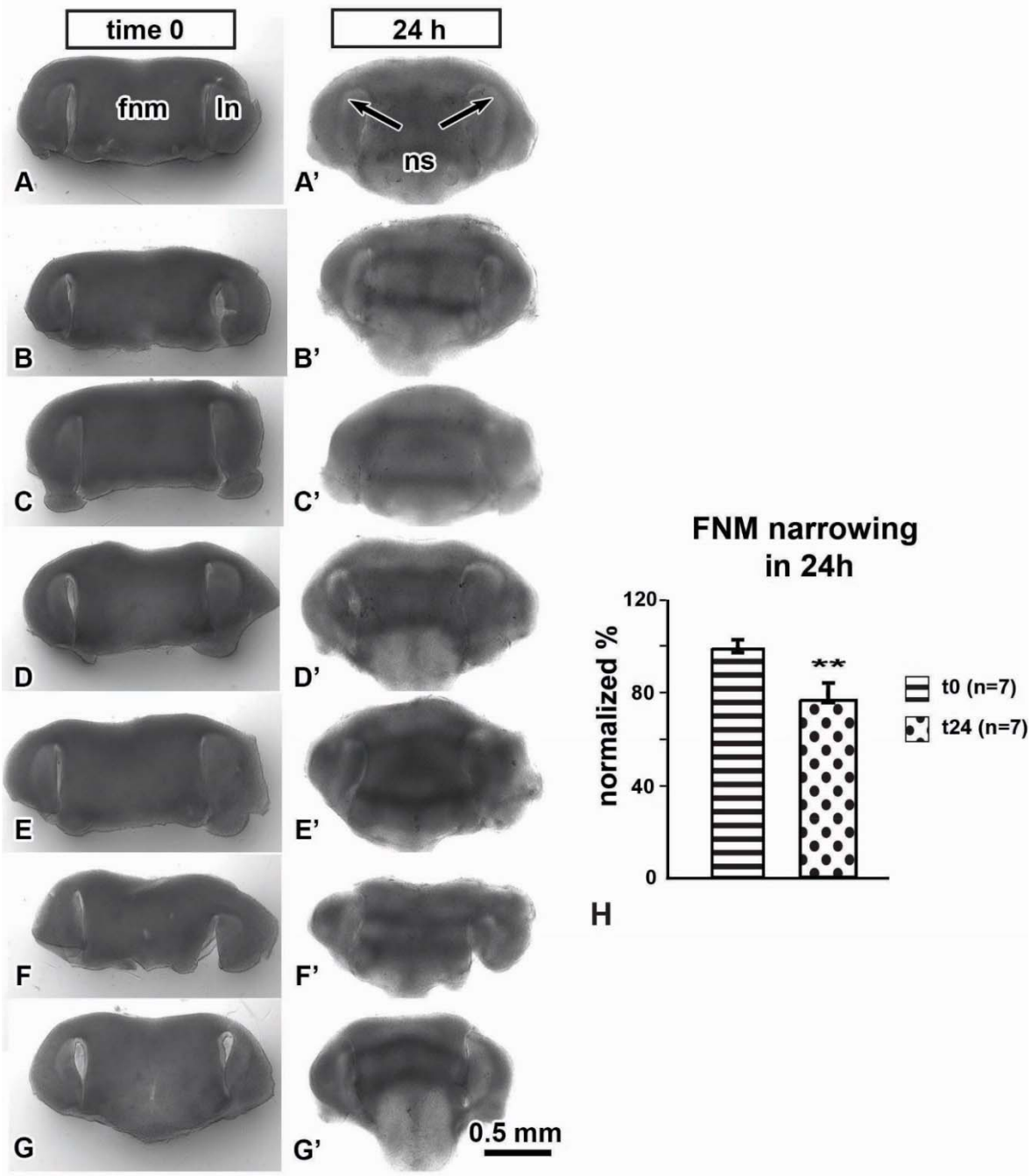

Figure S5. Images of frontonasal mass cultures before and after 24h of growth. A-G') The left column shows 7 individual cultures at the start of the growth period. The right column are the same cultures grown for 24h. H) Measurements of frontonasal mass width, midway through the nasal slit. Cultures were 20% narrower than at time zero.

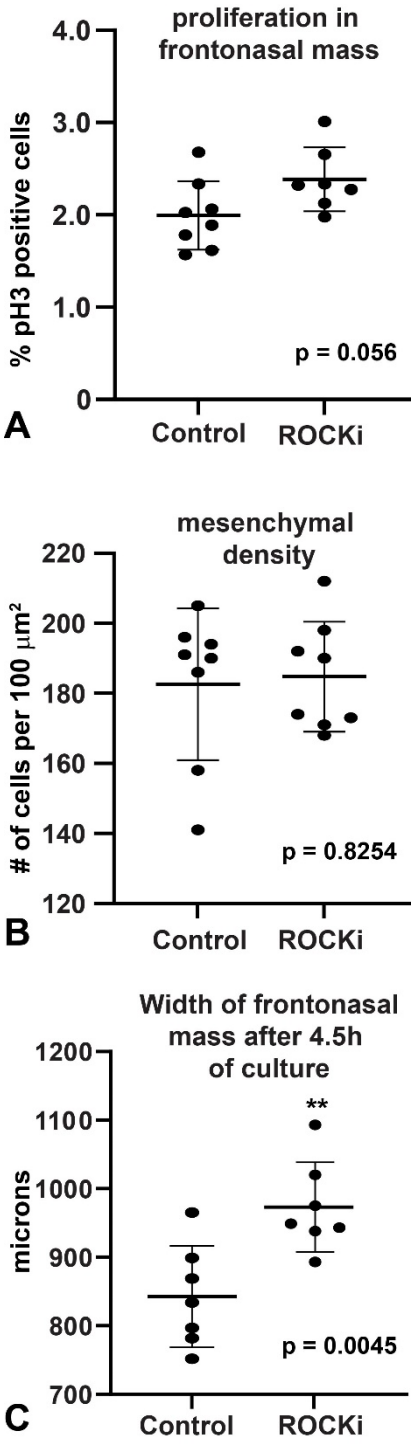

Figure S6. Analysis of frontonasal mass mesenchyme at the end of the imaging period. Cultures were grown in multi-well chamber slides on a layer of Matrigel for 4.5h, the period used for imaging. A) proliferation was assessed by counting the percentage of mitotic cells between the nasal slits. There was no significant difference between conditions. B) Cell density is unchanged by ROCKi treatment. C) Width of the frontonasal mass was measured at the midpoint of the nasal slits. There was a significant increase in width in the ROCKi treated cultures, similar to the results in 4G where cultures were measured after plating in Matrigel (took several hours). **=p< 0.01, determined by T-tests.

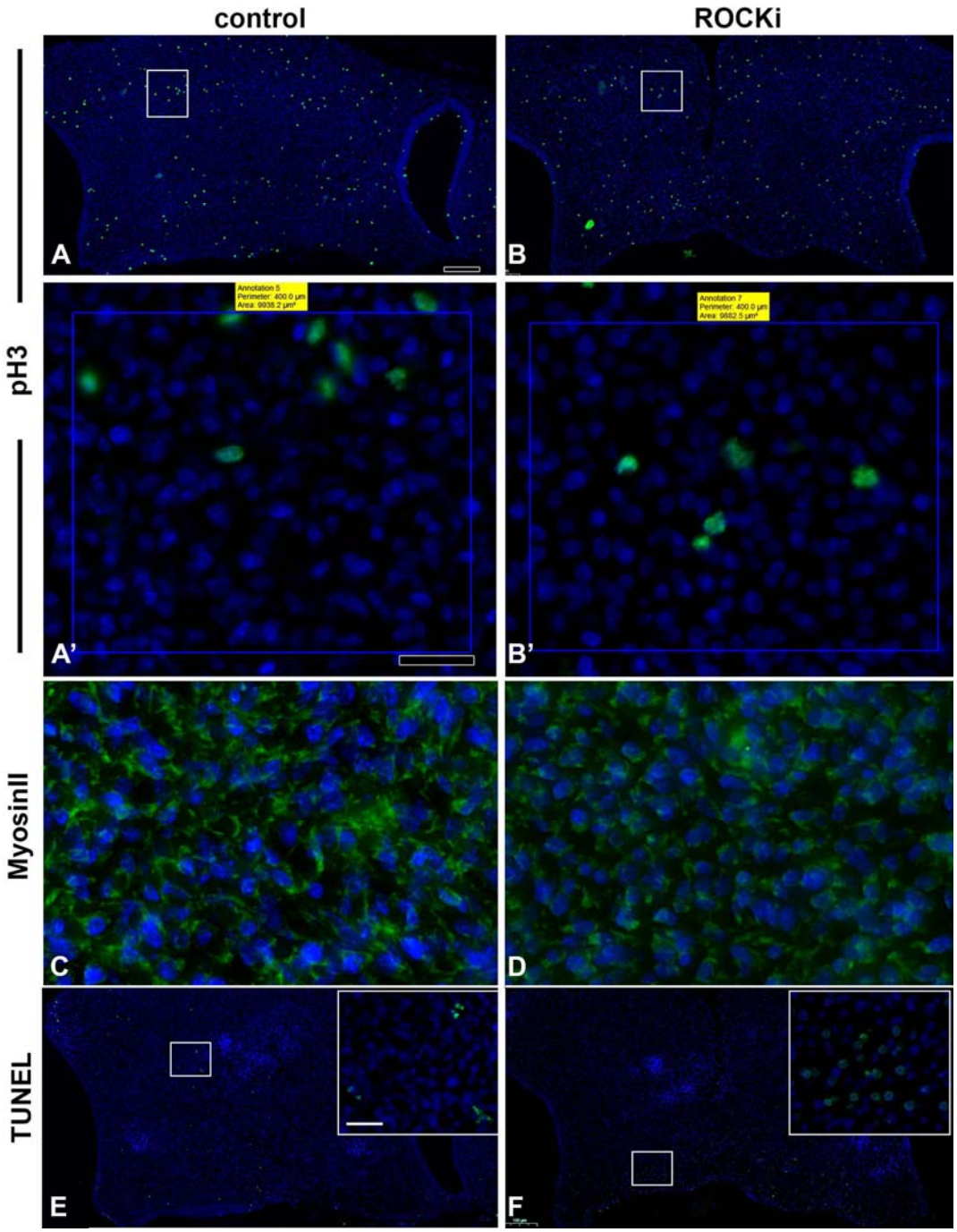

Figure S7. Frontonasal mass histology at the end of the imaging period. A, B) Staining of mitotic figures with pH3 was similar in control and treated cultures. A'B') an example of a 100 micron^2 area used to count cell density (inside the white box in A, B). C,D) Cytoskeletal staining with antibody to MyosinII non-muscle myosin. Cells are in contact with neighbouring cells and the matrix. E,F) Minimal detection of apoptotic cells in the control and treated cultures. Most of the signal is seen close the cut edges of the dissected frontonasl mass.
Scale bars = 100 microns for A,B,E,F. Bar in A' = 20 microns and applies to B',C,D and insets in E, F.

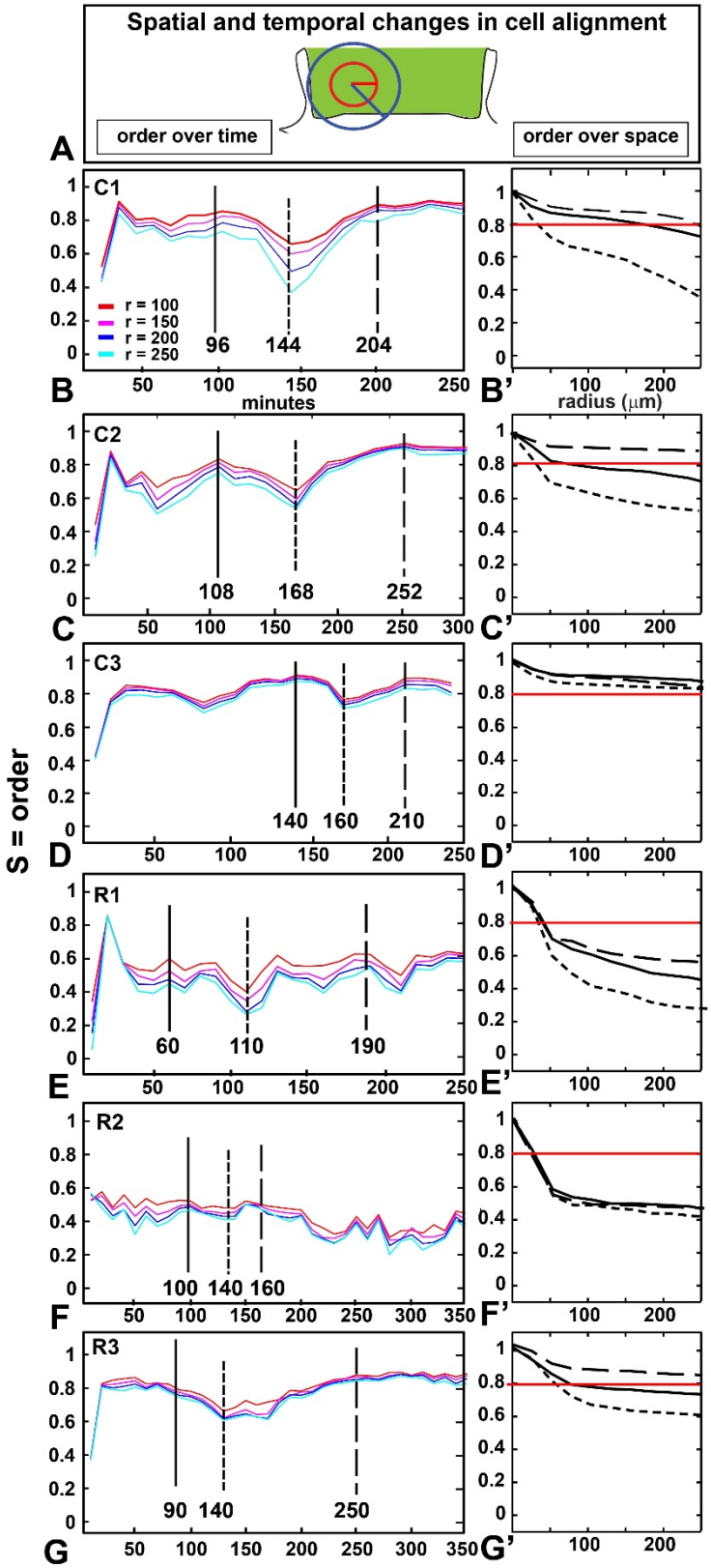

Figure S8. Spatial and temporal changes in cell alignment for all specimens at 10X: As in Fig 4H-I' but for the entire dataset. The direction of vectors at fixed time intervals was used to determine *S* as a function of time *t*. Vertical lines represent times of high directional order, disorder and order. Red circle is 100 μm in radius and blue circle is 200 μm radius. C1-C3 are controls and R1-R3 are ROCKi treated cultures.

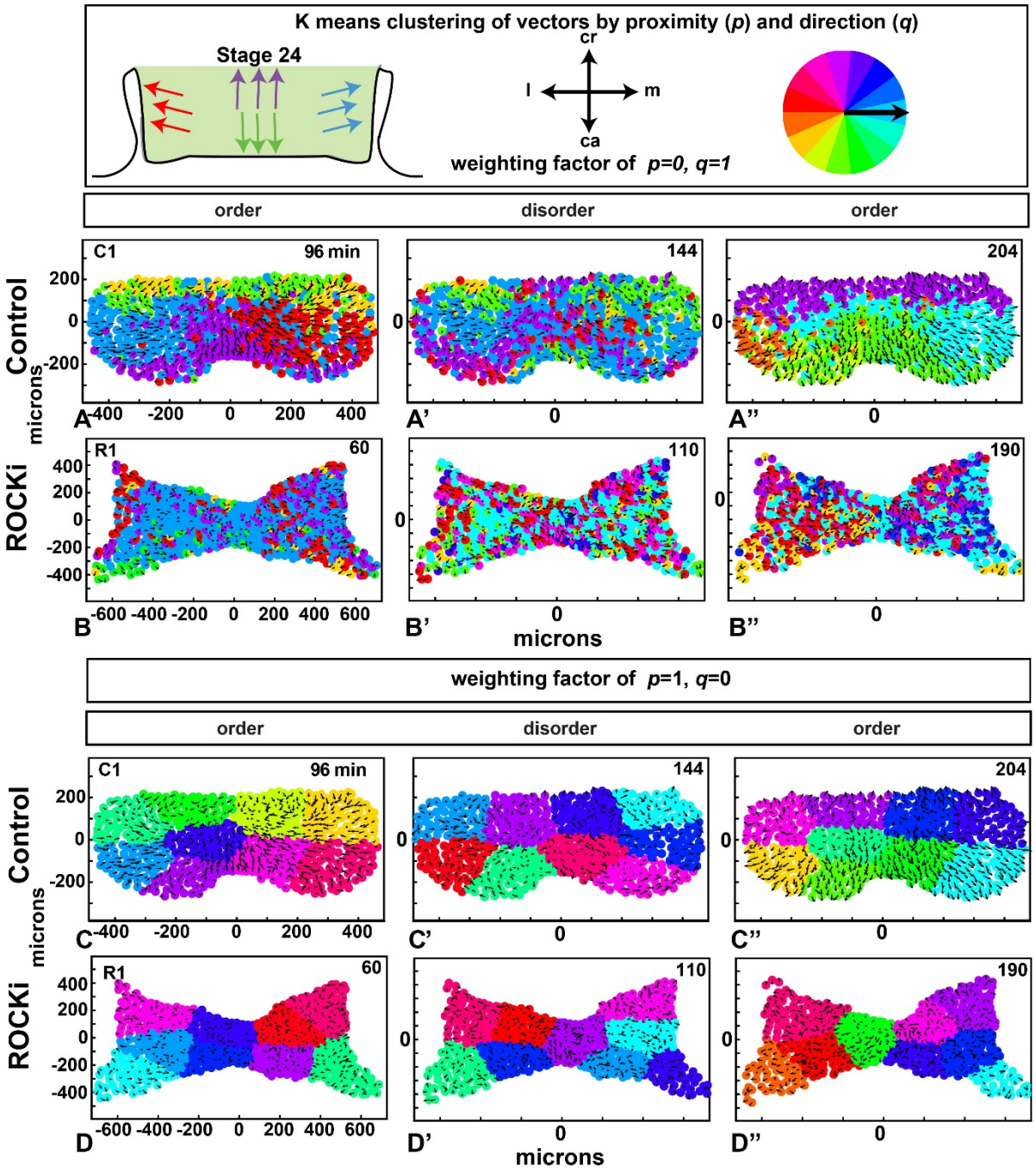

Figure S9. K-means clustering of vectors using Method 1 weighting on position and vector. A-B'') ** K-means clustering with relative weights position p=0, q=1) at the three time points of high order, disorder and order. The black arrows are cell velocity vectors. The colour wheel indicates the average direction of each cluster. When position is omitted and only vectors are considered the clusters are not distinct in controls. The ROCKi treated cultures have even less organization. **C,D'') Here weighting is entirely on position and not on vector. The clusters are in blocks because proximity is prioritized.

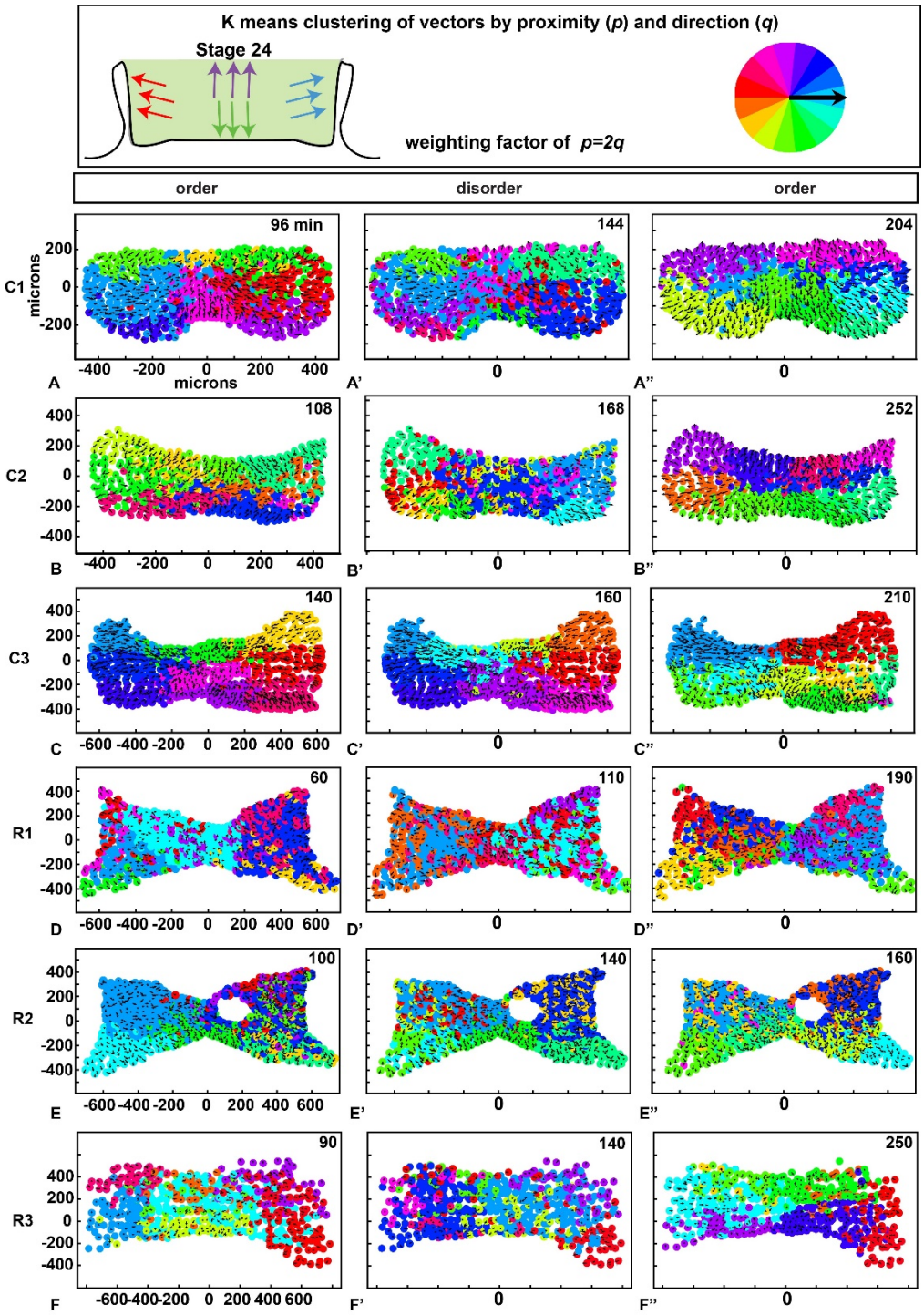

Figure S10. K-means clustering of vectors by Method 1. As in Fig 5A-B'', but for all specimens at 10X. K-means clustering with double the weighting for position compared to vector, p=2, q=1) at the three time points of high order, disorder and order (as in Supplementary Figure S5) The black arrows are cell velocity vectors. The colour wheel indicates the average direction of each cluster. **A-C'')** Clearer clusters are seen than if position was not considered. **D-F'')** Very few clear clusters can be seen in the ROCKi treated cultures.

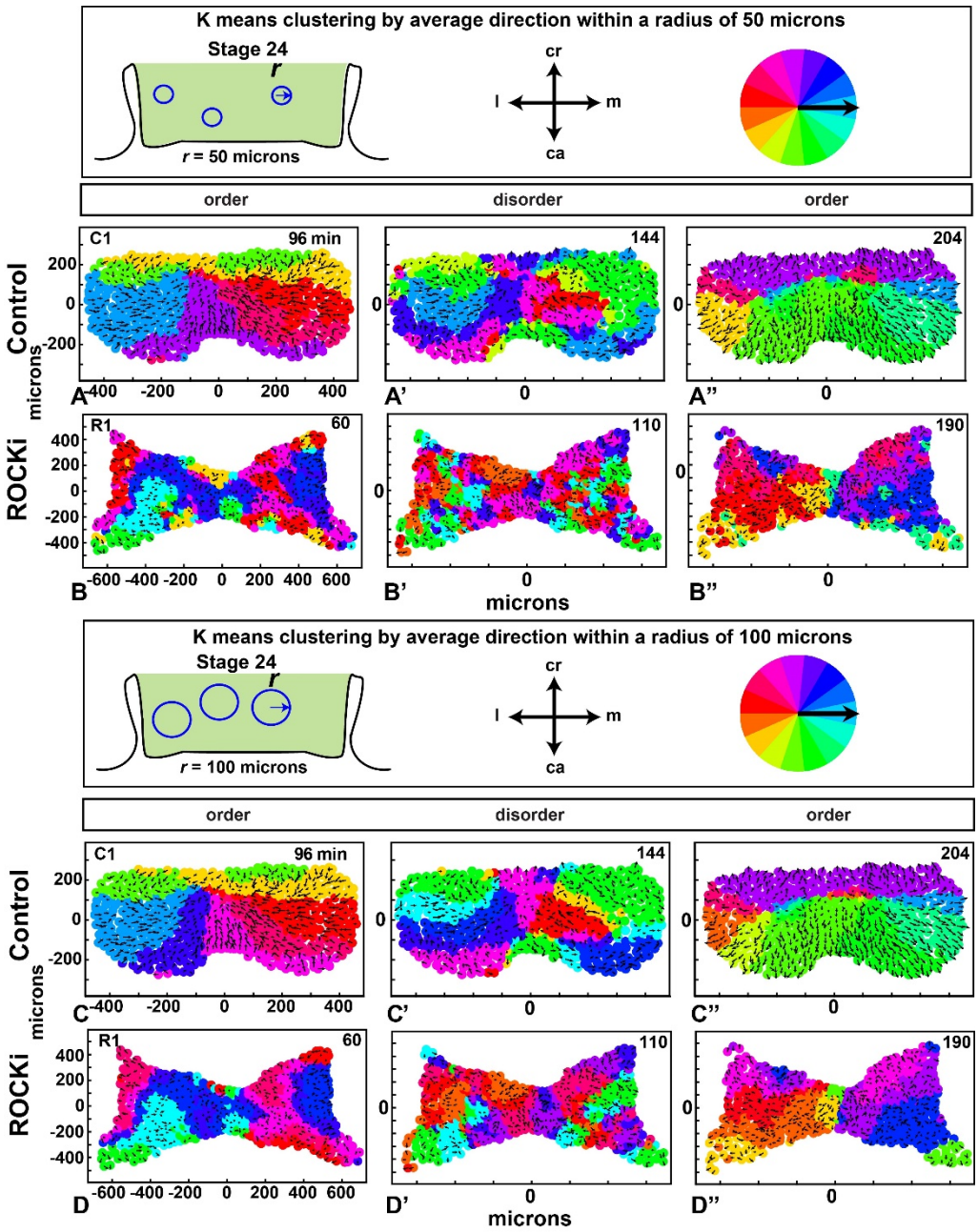

**Figure S11. K-means clustering of vectors by Method 2 (cells positioned within the same circle of specific diameter). A-B'') ** Multiple circles of 50 micron radius were place across the frontonasal mass and clusters built on those regions. Clear clusters are seen in th first time point (A) and last (A''). No clear clusters are seen in the ROCKi treated cultures. C-C'') with a larger diameter circle clear clusters are seen in controls. D-D'') The ROCKi treated cultures have a patchwork of cells with the same angle that are positioned on opposite sides of the frontonasal mass. For example see fuchsia cells on both right and left sides of the frontonasal mass in D and D''.

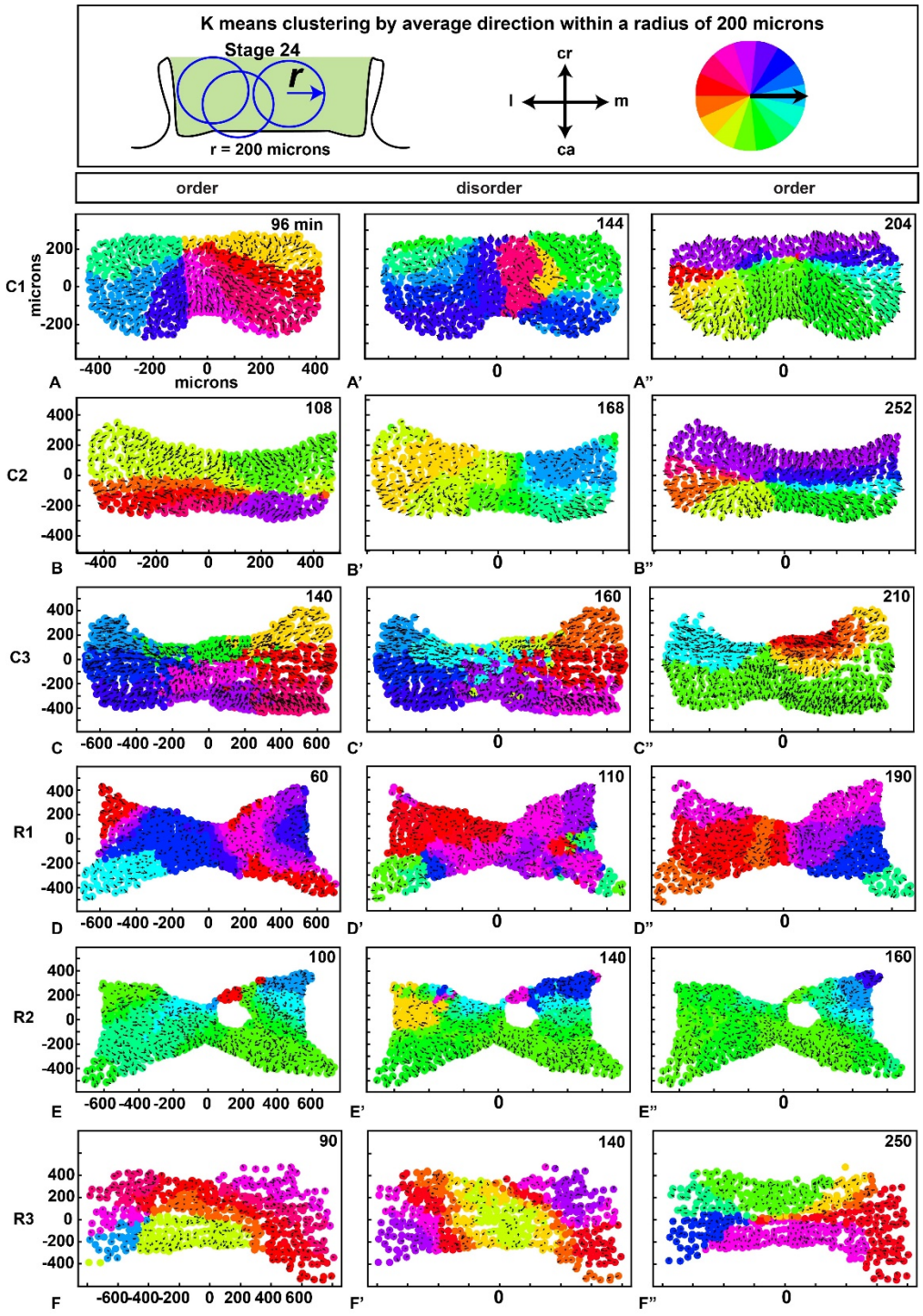

Figure S12. K-means clustering of vectors by Method 2. As in Fig 5C-D'', but for all specimens at 10X. K-means clustering by average direction (Method 2 with $r = 200$ µm) at the three time points of high order, disorder and order (as in Supplementary Figure S5) The black arrows are cell velocity vectors. Note that the colour wheel indicates the average direction of each cluster.

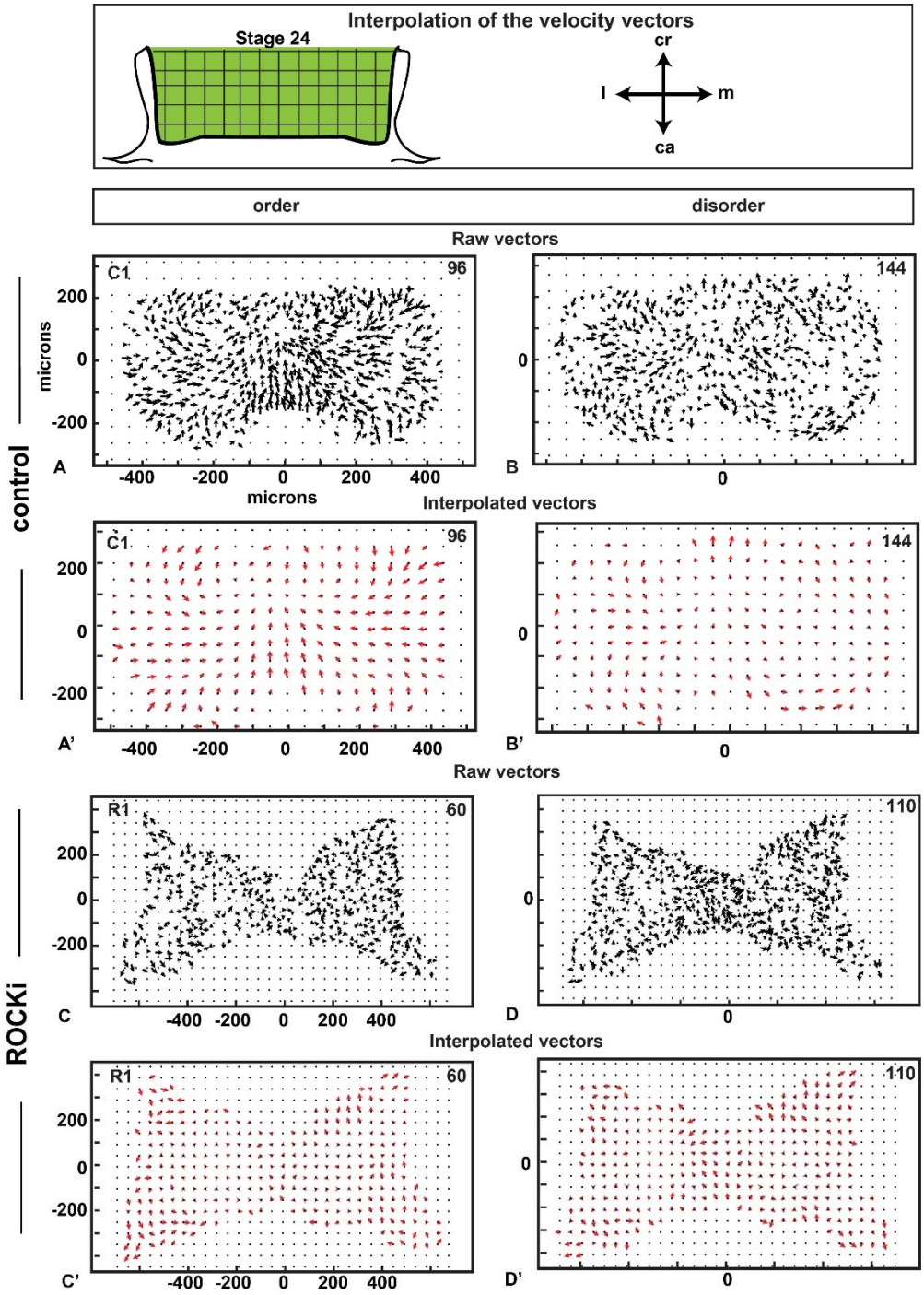

Figure S13. Interpolation or smoothing of data. Raw cell velocity vectors data (A,B,C,D in black) were interpolated by locally averaging data vectors over 50 µm radius neighborhoods. (Interpolation shown in red in A', B', C', D'). One control specimen (A-B') and one ROCKi treated specimen (C-D') are shown here, for ordered (A,A',C,C') and disordered states (B,B',D,D') Time-points in upper right corner, as in Fig 4H-I. The center of the frontonasal mass in controls tends to have smaller cellular velocities (shorter arrows). The ROCKi appears to have smaller velocities everywhere (slower cell motion).

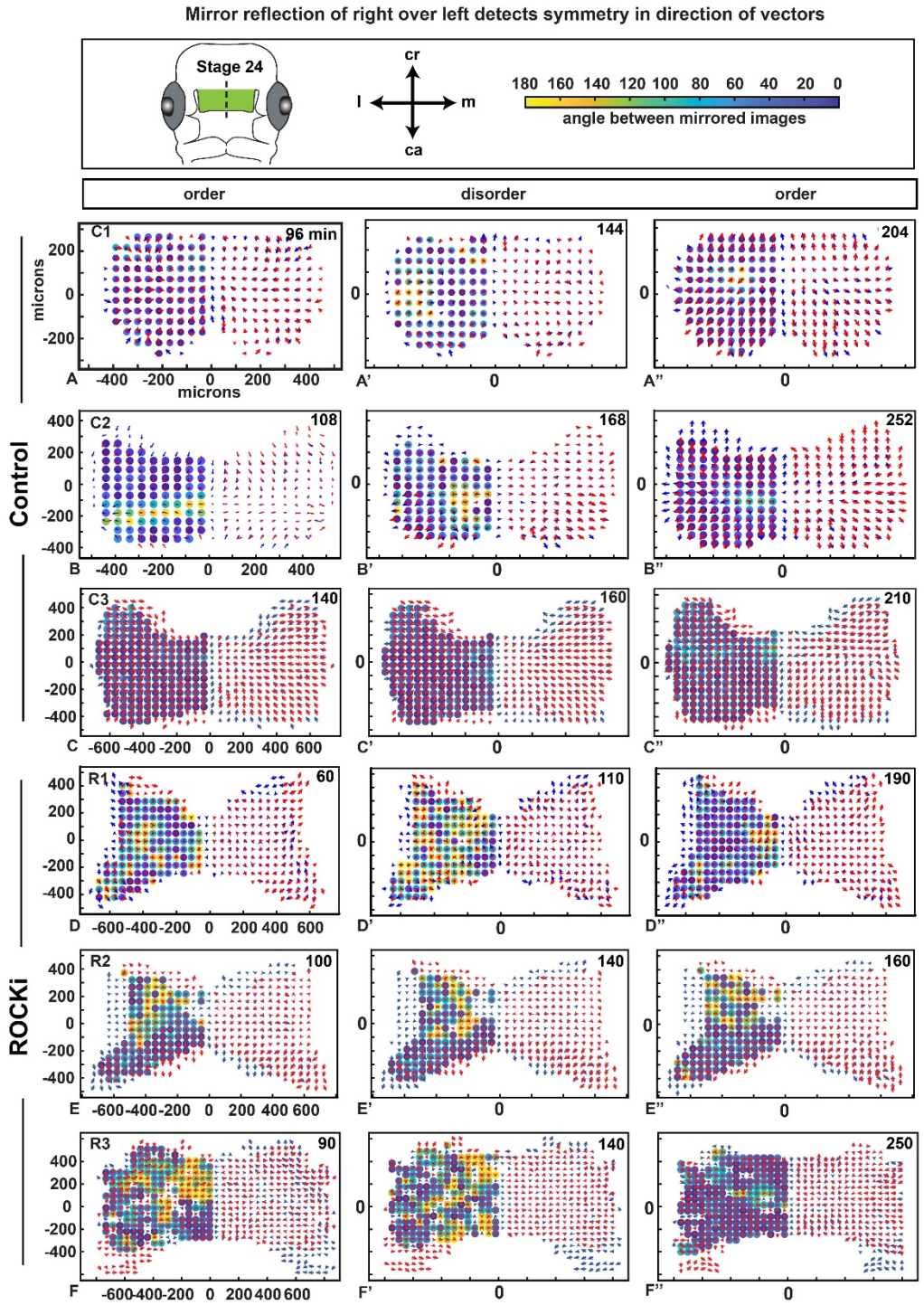

Figure S14. Right-left symmetry for all specimens.
Interpolated data (neighborhood averaging of 50 µm) at the three representative timepoints (Fig. S5) was used for the symmetry analyses. A-C'') Quantification of left-right symmetry in control cultures. There is high symmetry since the angle between mirrored images is very similar. D-F'') In ROCKi treated cultures there are mare areas with yellow circles or low symmetry, especially in the period of disorder.

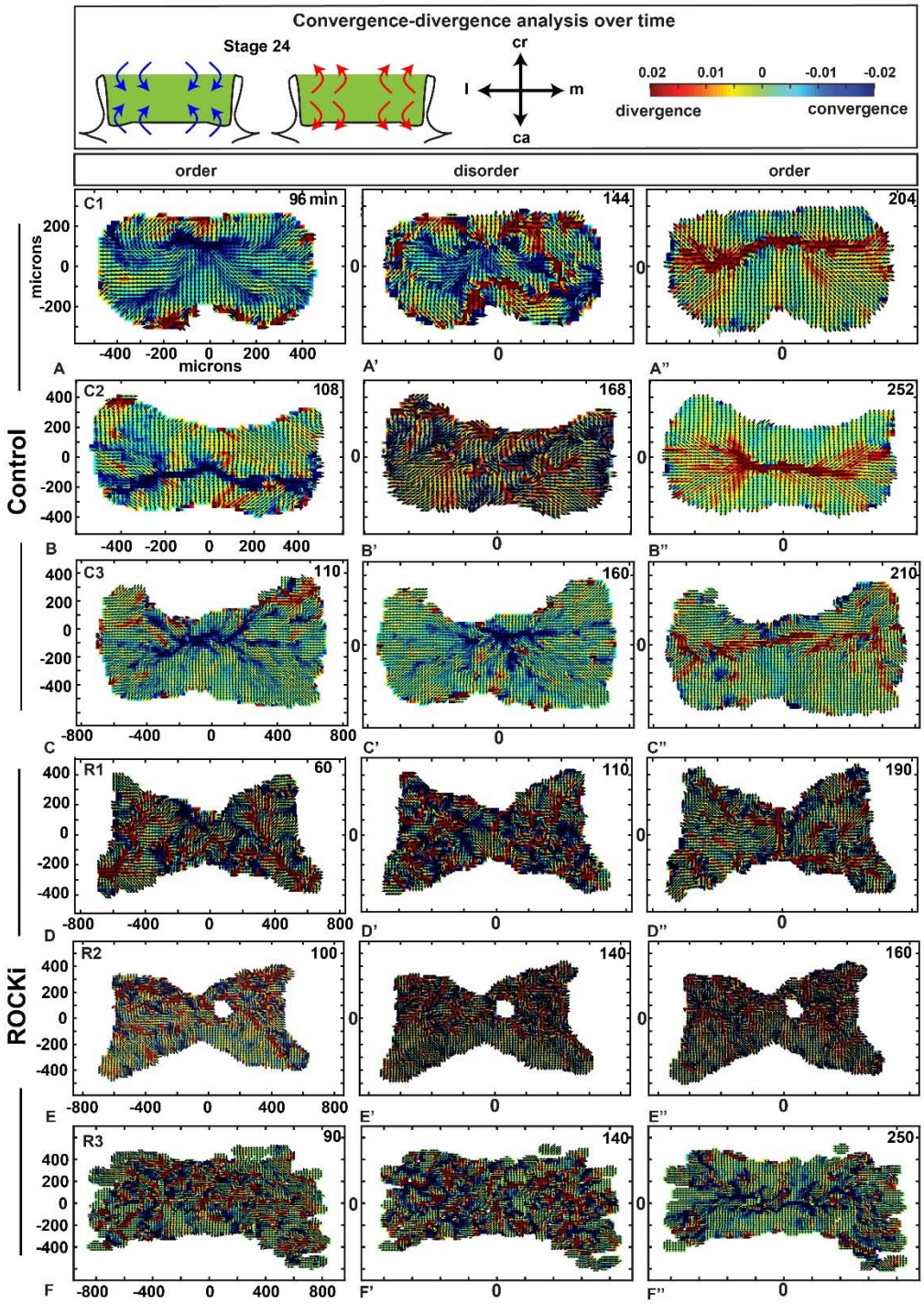

Figure S15. Convergence-divergence analysis for all specimens

A-C'') Control cultures have tendency for convergence towards the midline of the culture at the first period of order, but this changes to divergence by the end of the culture period. D-F'') In ROCKI treated cultures there is no clear pattern of divergence and convergence at any of the time points.

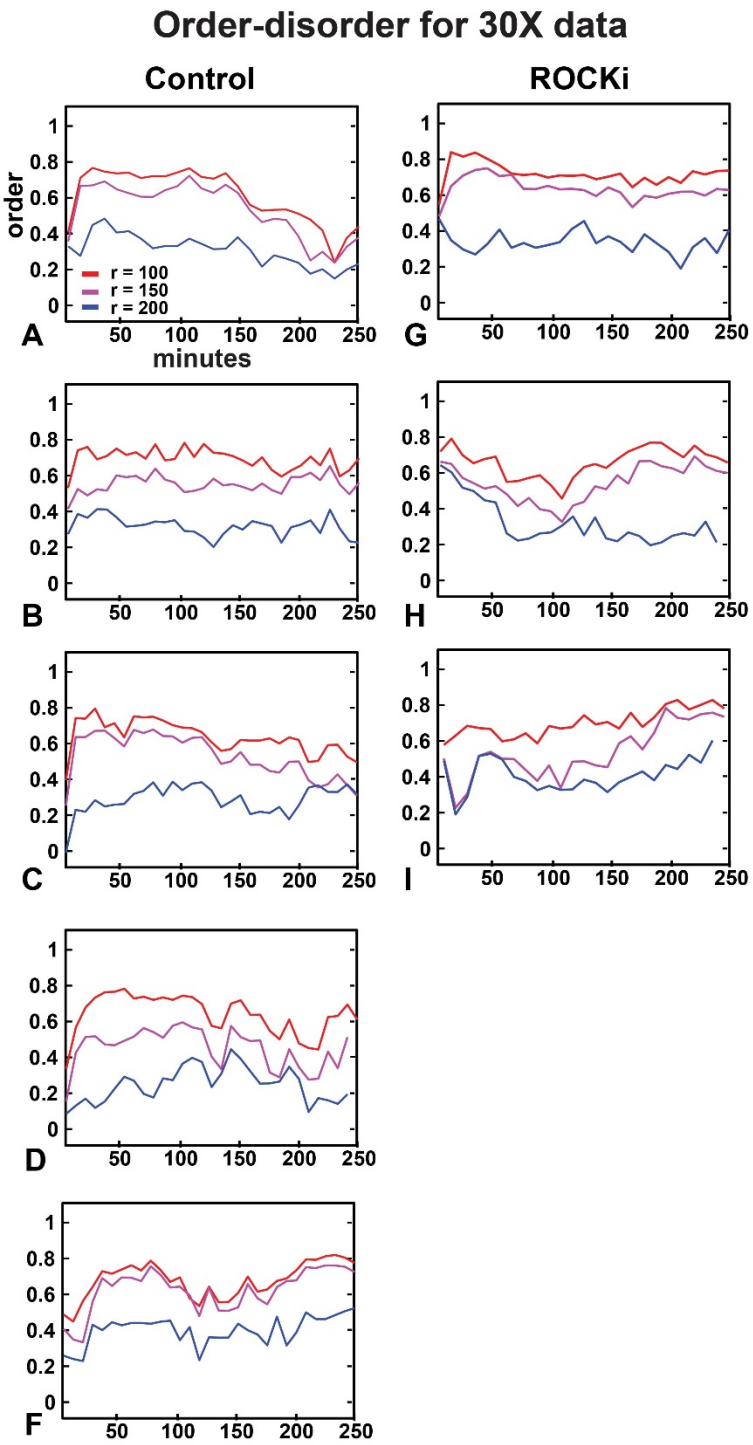

Figure S16. Order parameter over time at 30X. Time plots of the order parameter for the 30X data computed over various neighbourhoods (r = 100 - 500 μm). In contrast to Fig S5, no clear periodicity is seen in these graphs, demonstrating the fact that 10X data reveals trends not seen at higher magnification.

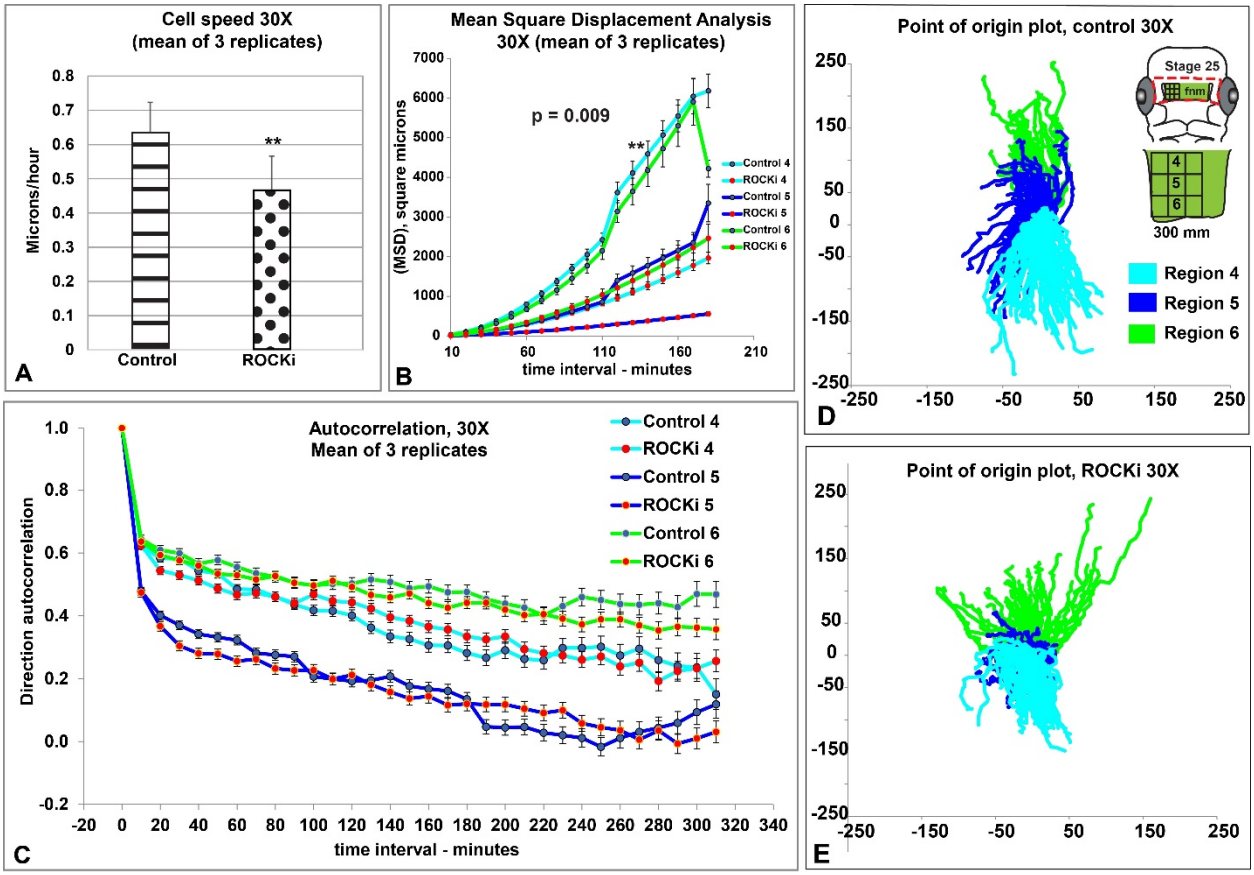

Figure S17. Individual cell measurements in the frontonasal mass.
The lateral third of the frontonasal mass was imaged. A grid was placed over the region and divided into 9 regions. Data from regions 4,5,6 is depicted and this data is representative of the other regions. Region 4 is at the cranial edge of the frontonasal mass, Region 5 is in the centre of the frontonasal mass, region 6 is close to the caudal edge. **A)** Instantaneous cell speed across all timepoints. Speeds for each culture were averaged and were considered 1 replicate. ROCKi treatment significantly decreased average cell speed. **B)** Displacement of cells in the controls was greater than for the equivalent region of the frontonasal mass in ROCKi treated cultures. P value is the result of ANOVA analysis comparing treated and control data. Regions are depicted in panel D. **D,E**) All cell tracks from the three replicates placed on a single point of origin. Axes are arbitrary. **D)** The tendency is for polarization of the cranial and caudal tracks (4,6) whether the centre has tracks that go cranial and caudally. **E)** The ROCK treatment causes more mediolateral spread. Also the tracks do not extend as far on the Y axis. Region 5 shows radial tracks that are relatively short.

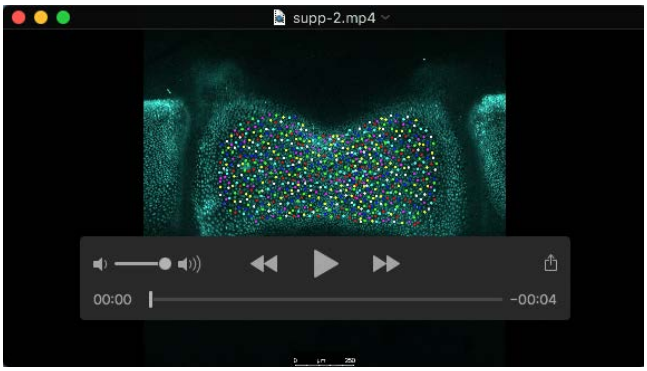

Movie 1. Time-lapse of stage 25 frontonasal mass dissected and cultured in control media. Nuclei were stained with Hoechst dye and imaged with confocal microscope, at 10X magnification (C1, control organ culture). Individual nuclei were tracked with manual tracking software. Dot is the end of the track and the tail is the trajectory of the movement. Cultures are oriented with the cranial edge uppermost in the image. The nasal slit is on the lateral sides of the tissue. The center of the frontonasal mass is relatively stationary in the center where cartilage will form at later stages.

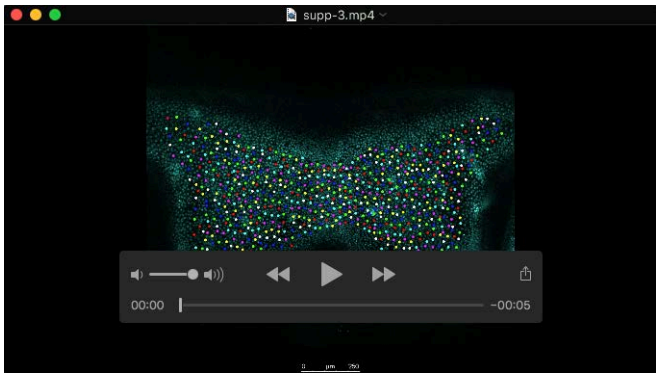

Movie 2. Time-lapse of stage 25 frontonasal mass dissected and cultured in ROCKi treated media. Nuclei were stained with Hoechst dye and imaged with confocal microscope, at 10X magnification (R1, ROCK inhibitor treatment organ culture). Tracks appear more disorganized and tissue failed to narrow in the mediolateral axis. The center of the frontonasal mass is relatively stationary in the center where cartilage will form at later stages, similar to control tissues.

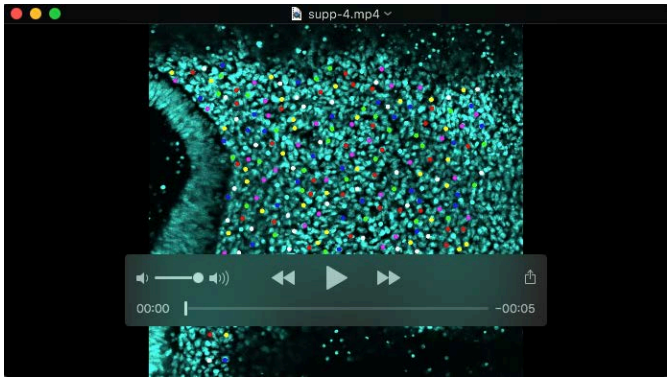

Movie 3. Time-lapse of stage 25 frontonasal mass dissected and cultured in control media. Nuclei were stained with Hoechst dye and imaged with confocal microscope, at 20X magnification with 1.5 optical zoom (C4, control organ culture).

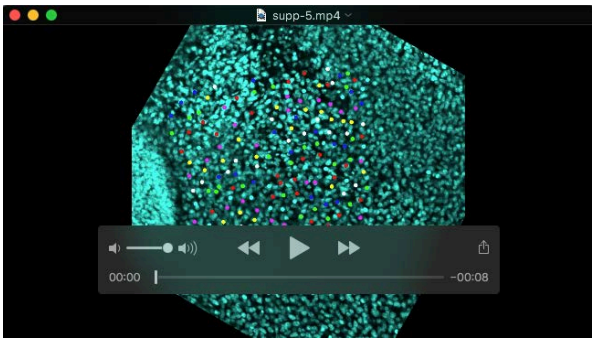

Movie 4. Time-lapse of stage 25 frontonasal mass dissected and cultured in ROCKi-treated media. Nuclei were stained with Hoechst dye and imaged with confocal microscope, at 20X magnification with 1.5 optical zoom (R4, organ culture).

Movie 5. Time-lapse of K-means clustering by Method 1 (by cell position and direction, relative weights p =2, q =1) for C1, control organ culture. Clusters are spatially diffuse.

Movie 6. As in Movie 5 but for the R1, ROCK inhibitor treatment organ culture. Clusters are even more spatially diffuse than in the controls.

Movie 7. Time-lapse of K-means clustering by Method 2 (considering only mean cell directions over a 200 µm radius) for C1 control organ culture. The maximum number of clusters is 7. The black arrows are the raw data for a given cell. Clusters of cells on the right and left sides and cranial-caudal axes are moving in opposite directions (see colour wheel) during the ordered times.

Movie 8. As in Movie 7. But for R1, ROCK inhibitor treatment organ culture. The maximum number of clusters is 7. The black arrows are the raw data for a given cell. In contrast to control samples, the ROCKi clusters are heterogeneous, lack neighbour similarity and are not organized into distinct regions. Clusters of cells with the same vector are not located in contiguous regions.

Movie 9. Time-lapse for divergence and convergence in the frontonasal mass for C1, control organ culture. Raw vector data was interpolated (averaged over 20 µm radius neighborhood) to facilitate the observation of complex patterns of divergence and convergence. We observed an initial band of convergence with several prominent branches at the lateral edges of the frontonasal mass followed by an overall direction change to divergence.

Movie 10. As in Movie 9 but for R1, ROCK inhibitor treatment organ culture. ROCKi treatment disrupted the patterns of convergence and divergence throughout the observations.

Movie 11.

Movie 12.

Supplementary Materials and Methods

OVERVIEW OF CELL TRACKING DATA ANALYSIS

ELISABETH RENS

Department of Mathematics, University of British Columbia, Vancouver, Canada

LEAH EDELSTEIN-KESHET

Department of Mathematics, University of British Columbia, Vancouver, Canada

Calculating velocity. The tracking data provides us with an x and y coordinate for each cell. Let i denote the cell number and $\mathbf{x}_i(t) = (x_i(t), y_i(t))$ its coordinates at time t. Then we approximate the velocity vector $\mathbf{v}_i(t) = (u_i(t), v_i(t))$ as follows:

$$u_i(t) = \frac{x_i(t) - x_i(t - \Delta t)}{\Delta t} \tag{1}$$

$$v_i(t) = \frac{y_i(t) - y_i(t - \Delta t)}{\Delta t} \tag{2}$$

where Δt=10 minutes, the time between each image.

Right-left symmetry. Here we examine the left-right (reflective) symmetry in the velocity field across the vertical midline of the samples (defined below). To better quantify symmetry, we first interpolate the velocity vectors to a fixed grid. This allows us to directly compare velocities at corresponding gridpoints. We defined a fixed grid with spacing $\Delta x = \Delta y = 50\mu$m. For each grid point, we then calculate the average ($\mathbf{v}_a$) of the n velocity vectors ($\mathbf{v}_i$) that are within a radius of 50μm.

These interpolated velocity vectors were then mirrored along the vertical midline. We define the mirroring axis for each specimen as $x = \frac{x_{\max}+x_{\min}}{2}$. Here, $x_{\max} = \max_{i,t} x_i(t)$ is the maximum coordinate of all cells over all time points in that specimen and similarly for the minimum coordinate. The mirrored velocities are defined as

$$\mathbf{v}_i^{\text{mirr}}(t) = (-u_i(t), v_i(t))$$

Now at each gridpoint, we calculate the difference in angle between $\mathbf{v}_i(t)$ and $\mathbf{v}_i^{\text{mirr}}(t)$ as $\alpha_i - \alpha_i^{\text{mirr}}$.

Divergence fields. To identify sources and sinks of movement, we calculate the divergence field. The divergence is defined as

$$\text{div } \mathbf{v}_i(t) = \nabla \cdot \mathbf{v}_i(t) = \frac{\partial u_i(t)}{\partial x} + \frac{\partial v_i(t)}{\partial y}$$

Negative divergence indicate a sink and positive divergence indicates a source. To approximate the spatial derivatives, we use a centered finite difference approximation. For cells at the boundary of the tissue, we use a forward/backward finite difference approximation. To be able to calculate the spatial derivatives of the velocity vectors sufficiently accurate, we first interpolated the velocity vectors on a much finer grid with spacing $\Delta x = \Delta y = 20\mu m$. At each gridpoint, we calculate the average velocity of the velocity vectors within a radius of 50 μ m of this gridpoint, again using equation **??**. We then calculated the divergence for this interpolated velocity field. Next, we also calculated the divergence for the normalized interpolated velocities. In the normalized case, all velocity vectors have length one, so that only the direction of motion is taken into account in calculating the divergence. For clarity, we show both the divergence of the interpolated velocity field and of the normalized field (unit vectors in the directions of the velocities).

The divergence field of the normalized vectors shows clear bands of divergence/convergence, that are usually more or less horizontal. We analyzed the divergence over time, by quantifying the divergence in these bands. First, we quantitatively identified the position of these bands as follows. We looked for a band of width r=60μm that had the most negative compared to positive divergence values, or the most positive compared to negative divergence values. Let $N_d(y)$ and $N_c(y)$ be defined as the number of grid points in the band around y that are either negative (diverging) or positive (converging):

$$N_d(y) = \#(x,y) : div(x, y-r \leq y \leq y+r) < 0$$

$$N_c(y) = \#(x,y) : div(x, y-r \leq y \leq y+r) > 0$$

Now the center of the band is found as

$$Y = \max_y \frac{\max\left(N_c(y), N_d(y)\right)}{\min\left(N_c(y), N_d(y)\right)}.$$

We imposed that the band should have a sufficient number of data points. This ensures that the band will not fall in the complete top or bottom of the tissue where not many data points are present. Let N be defined as

$$N = \max_y \#\text{gridpoints}(y)$$

the maximum number of data points existing in a row of the interpolated grid. We imposed that the number of data points within the band should be at least $0.7 \cdot N \cdot (\frac{2r}{20} + 1)$. A visual check confirmed that this simple algorithm identifies the location of the bands well. Next, we computed the average divergence over all data points in the located band:

$$\overline{div} = < div(x, Y-r \leq Y \leq Y+r) >,$$

where <> denotes the average. We used this measure to evaluate divergence over time.

Range of velocity alignment. We borrow the concept of an 'order parameter' from physics of liquid crystals [3], that has also been used in computational biology to quantify the alignment of cell shapes [5, 6, 8]. Here, we use this concept to quantify the extent of local alignment (of velocity vectors). We calculate the average velocity vector $\mathbf{v}_a^r(t)$ in a circular region with radius r around each cell i to obtain $\mathbf{n}_i^r(t)$ called the 'local director', which describes a local average direction within a range r of the cell i. The angle between this local director and cell i is denoted $\alpha_i^r(t)$. Now our 2D order parameter is calculated as

$$S(r,t) = \langle \cos(\alpha_i^r(t)) \rangle_i$$

If all cells are moving in exactly the same direction, then S will be close to 1. If cells move in various random directions, S will be close to zero. For a small r, S quantifies velocity alignment for cells close to each other, while for very large $r \approx 500\mu$m, S quantifies velocity alignment over the whole tissue. This 2D order parameter used here is slightly adapted from its original form ($S(r) = \langle \cos(2\alpha_i^r) \rangle_i$). In the alignment of molecules (physics) or cell shape (biology), a factor 2 is used because the agents do not have a direction, only an orientation (i.e. a direction of 0° is equivalent to 180°). Since we are studying velocities, direction is relevant to us, so we omit the factor 2. This can lead to negative values of S, because if a cell is moving in the opposite direction to all neighbouring cells, its $\alpha_i^r(t)$ will be 180° and thus $\cos(\alpha_i^r(t)) = -1$. Note that this order parameter, has been used to quantify velocity correlations over space before in [9, 7, 2].

Clustering. We use a weighted k-means clustering algorithm [1] to find regions of the tissue in which cells move similarly. The k-means clustering algorithm clusters objects based on the similarity between the variables of the objects, while selecting an optimal number of clusters. The algorithm clusters the objects by minimizing the 'distances' from objects to the 'centroid' of the clusters. The distance between an object and the centroid is defined as the sum over the Euclidean distance between their variables. In a weighted k-means clustering, the centroid of a cluster is weighted, i.e. the centroids of the cluster i are given by

$$Cij = \frac{\sum_k w_k V_{jk}}{\sum_k w_k}, \tag{3}$$

where k runs over all objects in the cluster, Vjk is the jth variable of the kth object and w_k the weight of object k. So, objects with higher weights are given more importance to the identity of the cluster.

In our case, the objects are cells and we want to cluster the cells based on similarity in velocity and position. We experimented with the following choices for variables and weights: 1) variables: direction of velocity and

positions of cells, weight: velocity of cells, and 2) variable: the 'local director' as described above with weight given by the local order. The details of the two different methods are described below. To avoid effects of noise and small artifacts, we restruct the number of clusters to no 9 or fewer. The algorithm usually gave an optimal number of clusters between 6 and 9.

Clustering angles and positions. To cluster cells based on their directions and positions, we define the following four variables V_1, V_2, V_3, V_4:

$$V_1 = q \cdot \frac{1+\cos(\alpha)}{2} \quad \text{(normalized velocity in x)} \tag{4}$$

$$V_2 = q \cdot \frac{1+\sin(\alpha)}{2} \quad \text{(normalized velocity in y)} \tag{5}$$

$$V_3 = p \cdot \frac{x - \min_i x_i(t)}{\max_i x_i(t) - \min_i x_i(t)} \quad \text{(normalized x coordinate)} \tag{6}$$

$$V_4 = p \cdot \frac{y - \min_i y_i(t)}{\max_i y_i(t) - \min_i y_i(t)} \quad \text{(normalized y coordinate)} \tag{7}$$

describing the position and directions of cells. The normalization ensures equal weighting of all variables ($0 \leq C1, C2, C3, C4 \leq 1$) if $p = 1$ and $q = 1$. We set $q = 1$. By varying p, we can assign more or less weight to the positions in comparison to the directions of the cells. For small p, the clustering will be mainly done on the angles, so that cells far apart can be clustered together. For larger p, cells are less likely to become clustered together if they are spatially far apart. Finally, the weights are given by $w_i = |\mathbf{v}_i(t)|$. This ensures that cells with higher velocities are assigned more confidence (data of cells with low velocities is more prone to errors).

We experimented with a variety of clustering options, by (1) varying p, (2) clustering only V_1 and V_2 (equivalent to $p = 0$), (3) clustering only V_3 and V_4 (q=0,p=1). We compared our clusters of large p ($p = 2, p = 5$) to case (3), to ensure that V_1, V_2 are at least given some weight and the clustering in not too biased towards positions. We found that $p = 2$ gives the best results. Directions are well clustered and, at the same time, position is taken into account, so that the clusters are connected in space.

Clustering the local director. Instead of clustering the direction and positions, here we cluster the local average orientation of cells given by the local director $\mathbf{n}_i^r(t)$ as described before. Let's call this local orientation γ. Now we cluster two variables V_1 and V_2 given by

$$V_1 = \frac{1+\cos(\gamma)}{2} \quad \text{(normalized velocity in x of local director)} \tag{8}$$

$$V_2 = \frac{1+\sin(\gamma)}{2} \quad \text{(normalized velocity in y of local director)} \tag{9}$$

Here the weights are given by

$$w_i = \frac{1 + \cos(\alpha_i^r(t))}{2}$$

where $0 \leq w_i \leq 1$ and $\alpha_i^r(t)$ is the angle between the local director and cell i. If w_i is large, this means that the direction of the cell is similar to the average orientation and thus will be given a higher confidence.

By varying r in this clustering method, we basically smooth the velocity vector field over a range r. In contrast to the first method, this clustering method does not take the positions of cells into account explicitely. However, this 'smoothing' ensures that two cells far apart, but moving in a similar direction, will not be clustered together, because the average direction within these two different regions are different. We performed this clustering method for $r = 0, 50, 100, 200, 300, 400\mu$m. If $r = 0$, then the local director is the same as the direction of the cell and $w = 1$ for all cells. This means we are clustering the original directions of the cell, and this case is equivalent to our first clustering method with $p = 0$. We found that $r = 200$ gives good results, as it is a biologically relevant [4, 10] and the clusters are connected in space.

References

[1] Margareta Ackerman, Shai Ben-David, Simina Brânzei, and David Loker. Weighted clustering. In *AAAI*, 2012.

[2] Thomas E Angelini, Edouard Hannezo, Xavier Trepat, Jeffrey J Fredberg, and David A Weitz. Cell migration driven by cooperative substrate deformation patterns. *Physical review letters*, 104(16):168104, 2010.

[3] PG de Gennes. J. prost, the physics of. *Liquid Crystals*, 1993.

[4] Norihisa Higashihori, Marcela Buchtová, and Joy M Richman. The function and regulation of tbx22 in avian frontonasal morphogenesis. *Developmental Dynamics*, 239(2):458–473, 2010.

[5] Ralf Kemkemer, Simon Jungbauer, Dieter Kaufmann, and Hans Gruler. Cell orientation by a microgrooved substrate can be predicted by automatic control theory. *Biophysical journal*, 90(12):4701–4711, 2006.

[6] Margriet M Palm and Roeland MH Merks. Vascular networks due to dynamically arrested crystalline ordering of elongated cells. *Physical Review E*, 87(1):012725, 2013.

[7] Laurence Petitjean, Myriam Reffay, Erwan Grasland-Mongrain, Mathieu Poujade, Benoıt Ladoux, Axel Buguin, and Pascal Silberzan. Velocity fields in a collectively migrating epithelium. *Biophysical journal*, 98(9):1790–1800, 2010.

[8] Elisabeth G Rens and Roeland M H Merks. Cell contractility facilitates alignment of cells and tissues to static uniaxial stretch. *Biophysical Journal*, 112(4):755–766, 2017.

[9] Benjamin Slater, Camila Londono, and Alison P McGuigan. An algorithm to quantify correlated collective cell migration behavior. *Biotechniques*, 54(2):87–92, 2013.

[10] Heather L Szabo-Rogers, Poongodi Geetha-Loganathan, Suresh Nimmagadda, Kathy K Fu, and Joy M Richman. Fgf signals from the nasal pit are necessary for normal facial morphogenesis. *Developmental biology*, 318(2):289–302, 2008.